



TECHNISCHE
UNIVERSITÄT
WIEN



HEPHY
INSTITUT FÜR
HOCHENERGIEPHYSIK

4H-Silicon carbide as real time monitor for high-intensity ion beams

DIPLOMA THESIS

Conducted in partial fulfillment of the requirements for the degree of a
Diplom-Ingenieur (Dipl.-Ing.)

supervised by

Univ.Prof. Dipl.-Phys. Dr.rer.nat. Jochen Schieck
Univ.Lektor Dipl.-Ing. Dr.techn. Thomas Bergauer

submitted at the

TU Wien
Faculty of Electrical Engineering and Information Technology

by

Manuel Christanell
Matriculation number 01327431

Vienna, September 2021

Detector development Group

A-1050 Wien, Nikolsdorfer Gasse 18, Internet: <https://www.oeaw.ac.at/en/hephy>

Abstract

Silicon carbide as a particle detector material offers various advantages over the use of other materials. For instance, it has a higher radiation hardness and produces a lower dark current than silicon, and larger detector areas are realizable than with CVD (chemical vapor deposition) diamond. Some of these properties make it particularly interesting for detecting high-intensity particle beams, such as those used in ion beam therapy for cancer treatment.

To learn more about the signal properties of silicon carbide detectors, a planar single-channel 4H-silicon carbide sensor was investigated in this project and compared to other sensors made of CVD diamond and silicon. The first step was to simulate the output signals of all sensors when they are penetrated by MIP particles (minimum ionizing particles) in a program called Weightfield2. Then measurements were performed with an alpha source, a beta source, and at the MedAustron proton beam, where different particle energies (60-800 MeV) and rates (kHz-GHz) were used. A setup created exclusively for this project was employed to record the generated detector signals remotely via a computer and simultaneously display and store the corresponding particle rates.

The three sensors were operated with the UCSC (University of California Santa Cruz) board, which forms the readout electronics and consists mainly of a transimpedance amplifier. To investigate its influence on the signal output, the board circuit was simulated and examined in the program Qucs.

The results show that the signal-to-noise ratio of the used silicon carbide detector system is at the moment not sufficient to detect individual MIP particles reliably. This is due to the low signal amplitudes, which were measured to be in average roughly only a sixteenth of the signal amplitudes of the silicon sensor. In addition, noise is induced by the components of the readout electronics.

The findings gained in this project serve as the base for the development of an entirely new readout circuit, which, through various precautions and a realization implemented in an ASIC (application-specific integrated circuit), should make it possible in the future to increase the SNR to such an extent that a reliable detection is possible.

Kurzzusammenfassung

Der Einsatz von Siliziumkarbid als Teilchendetektormaterial bietet diverse Vorteile gegenüber der Verwendung von anderen Materialien. So weist Siliziumkarbid eine höhere Strahlungshärte und einen kleineren Dunkelstrom als Silizium auf. Zudem lassen sich damit größere Detektorflächen als mit CVD (chemical vapor deposition) Diamant realisieren. Seine Eigenschaften machen das Material für die Detektion von hochintensiven Teilchenstrahlen, wie sie zum Beispiel bei der Krebsbehandlungen durch Ionenstrahltherapie eingesetzt, besonders interessant.

Um mehr über die Signaleigenschaften solcher Siliziumkarbid-Detektoren zu erfahren, wurde in diesem Projekt ein planarer einkanal 4H-Siliziumkarbid Sensor untersucht und mit anderen Sensoren aus CVD Diamant und Silizium verglichen. Hierbei wurden die Ausgangssignale aller Sensoren beim Beschuss durch MIP (minimum ionizing particles) Teilchen in einem Programm namens Weightfield2 simuliert. Dann wurden Messungen mit einer Alpha-Quelle, einer Beta-Quelle und einem Protonen-Strahl (im Forschungs- und Krebsbehandlungszentrum MedAustron) mit verschiedenen Teilchenenergien (60-800 MeV) und Raten (kHz-GHz) durchgeführt. Eingesetzt wurde dabei ein Messaufbau, welcher eigens für diesen Zwecke entwickelt wurde und es ermöglicht, die erzeugten Detektorsignale ferngesteuert über einen Computer aufzuzeichnen und gleichzeitig die Teilchenraten darzustellen und abzuspeichern.

Bei allen Messungen wurden die drei Sensoren mithilfe des UCSC (University of California Santa Cruz) board ausgelesen, welches zum größten Teil aus einem Transimpedanzverstärker besteht. Um dessen Einfluss auf das Ausgangsverhalten zu untersuchen, wurde die Schaltung des Boards in dem Programm Qucs simuliert und untersucht.

Die Ergebnisse zeigen, dass das Signal-Rausch-Verhältnis des verwendeten Siliziumkarbid-Detektorsystems momentan nicht ausreicht, um einzelne MIP Teilchen verlässlich zu detektieren. Probleme bereiten die geringen Signalamplituden, welche gemessen und genähert im Durchschnitt nur etwa ein sechzehntel der Signalamplituden des untersuchten Silizium-Sensors betragen. Hinzu kommen Rauschanteile, die von den Bauteilen der Ausleseelektronik induziert werden.

Die in diesem Projekt erlangten Erkenntnisse dienen als Basis für eine Weiterentwicklung der Ausleseelektronik, welche es durch diverse Vorkehrungen und eine in ASIC (application-specific integrated circuit) implementierte Realisierung in Zukunft möglich machen soll, den SNR so weit zu erhöhen, dass eine zuverlässige Detektierung möglich wird.

Contents

1	Introduction	1
2	Theoretical background	3
2.1	Energy loss of charged particles in matter	3
2.1.1	Scattering on electrons and nuclei	3
2.1.2	Bremsstrahlung	4
2.1.3	Bethe-Bloch Formula	5
2.1.4	Stochastic fluctuation in the energy deposition	7
2.2	Particle Therapy	8
2.2.1	Treatment plans	8
2.2.2	Intensities	9
2.3	Semiconductor Detectors	10
2.3.1	Function principle	10
2.3.2	Charge carrier mobility	12
2.3.3	Signal duration	13
2.3.4	Pile-up effect	14
2.4	Radioactive sources	15
2.4.1	Americium-241	16
2.4.2	Strontium-90	19
3	Solid state sensors	22
3.1	Silicon sensor	22
3.2	Diamond sensor	24
3.3	Silicon carbide	25
3.4	LGAD sensor	27
3.5	Characterization measurements	29
3.6	Sensor simulations	32
3.6.1	Weightfield2	32
3.6.2	Results	34
4	Readout electronics	35
4.1	The UCSC board	36
4.1.1	Theoretical analysis	38
4.2	Circuit simulations	38
4.2.1	Qucs	39
4.2.2	Results	41

5	Measurements	43
5.1	Measurements with radioactive sources	43
5.1.1	Americium-241	44
	Setup	44
	Results	45
5.1.2	Beta telescope	47
	Setup	47
	Results	48
5.2	Measurements at MedAustron	52
5.2.1	Setup	53
5.2.2	Results	56
6	Conclusion and outlook	63
7	Acknowledgement	65
	Appendices	67
	List of Figures	67
	List of Tables	69

1 Introduction

The therapy of cancer with ions beams is an attractive alternative to conventional radiotherapy treatments [1][2]. The advantage of using such beams lies in the particular energy deposition curve of heavy charged particles like protons or carbon ions. Unlike photons, which lose a considerable amount of energy before they even reach the tumor, protons can be accelerated to the point where their maximum energy deposition per path length is precisely at the deep of the tumor. This allows the selective termination of cancer cells and reduces the damage done to healthy tissue [2]. To treat patients here in a reasonable time, particle intensities as high as 10^{10} ions/second are necessary [3]. Additionally, the particle beam properties must be frequently monitored to ensure a safe treatment. The detector material used to monitor such persistently high-intensity particle beams must have particular properties like a high radiation hardness and a high charge carrier mobility. In addition, detector areas, which cover the whole beam, must be producible.

In MedAustron, a research and cancer treatment facility located in Wiener Neustadt (Austria), SFX scintillating fiber sensors are used to determine the beam properties. The downside of those sensors is that they are starting to suffer from radiation damages due to the high particle intensities used in the treatments. This could limit their functionality in the future. Therefore, this project aims to find a possible replacement for those detectors, which could also be used in general applications working in the high-intensity ion beam range.

A promising and rather new sensor semiconductor material candidate is silicon carbide. Silicon carbide has some advantages compared to other materials like the state-of-the-art material for solid-state position-sensitive detectors, silicon. The higher bandgap compared to silicon reduces the dark current and eliminates the need for cooling even in harsh environments [4]. The higher radiation hardness leads to fewer material alterations, resulting in a longer lifetime, especially under high radiation conditions [5]. The properties of silicon carbide make the material also interesting for power devices in the chip industry, which reduces the manufacturing costs and makes large area detectors available and affordable. This is in contrast to diamond sensors produced in the chemical vapor deposition procedure (CVD diamond), which are limited to a square of a few cm^2 .

Because of the previously mentioned advantages, the possibility of 4H-silicon carbide, one polytype of SiC, as a material for particle detectors, especially but not exclusively for high-intensity ion beams, was examined in this project. In addition, requirements concerning a future silicon carbide readout system were studied. The sensor used for this purpose is a 4H-silicon carbide single-channel epitaxial diode.

A single channel planar silicon and a single channel CVD diamond detector were operated under the same testing conditions as the silicon carbide sensor to exhibit the differences between the produced output signals. The investigation includes the determination of the sensor capacitance-voltage and current-voltage relations of all three sensors, the simulation of those detectors in a program called Weightfield2, and measurements in the laboratory with an alpha and a beta source. Additionally, experiments in the beamline of MedAustron with particles energies from 62 MeV up to 800 MeV and intensities starting from 3 kHz up to 10^{10} particles per 5 s spill, were conducted. In all those measurements, the sensor signal forms produced by the penetrating particles were captured after being processed by the readout electronics. Furthermore, a particle rate and time-over-threshold determination were implemented in the setup used at MedAustron.

All sensors of this project were operated with the UCSC board, which is a readout system consisting mainly of a transimpedance amplifier. To draw conclusions about the detectors from the board's output voltage signal, the properties of the board had to be determined first. This was done in theoretical analysis and through simulations in the program Qucs.

2 Theoretical background

Charged particles leave a trail of ionized electrons and holes when passing through matter. Those tracks make it possible to detect the particles with a whole range of different detector systems.[6]

- There are gaseous tracking systems, where the excited electrons are accelerated in an electric field towards electrodes producing so a measurable signal.[7]
- Detector systems based on inorganic scintillators, in which the ionization of electrons leads by collision processes to the emission of detectable photons.[8]
- Or semiconductors, where the charged particle excites electrons, which can lift them from the valence band into the conduction band, leaving back holes. If then a voltage is applied, the excited electrons and holes can be extracted and produce so a measurable current flow.[9]

In all those detector systems, the signal height depends on the number of ionized electrons. Except in detector systems operated in geiger mode, the number of ionized electrons in turn is proportional to the energy loss of the particles due to ionization processes while traveling through the sensor material. Therefore, to estimate the behavior of such sensors it is essential to know the energy loss of the particles in matter.

2.1 Energy loss of charged particles in matter

Charged particles can lose energy in different ways when penetrating matter. Depending on the particle type and energy, some processes are more dominant than others. A few of those interaction processes are described in this chapter more precisely.

2.1.1 Scattering on electrons and nuclei

When a heavy charged particle interacts with bound electrons, inelastic scattering occurs (Figure 2.1a). In this process, the particle transfers a part of its energy to the electron, which then will be excited or ionized. Due to the low electron mass, the momentum of the particle is hardly changed.[10]

On the other hand, in the elastic scattering with atomic nuclei, the particle's momentum is changed (Figure 2.1b). This is because of the relatively large mass of the nucleus compared to the particle mass. Since the scattering at nuclei occurs more rarely, most energy is transferred to the matter by scattering with the electrons. Except for very low energies and high particle masses the nuclei scattering can therefore be neglected.[11]

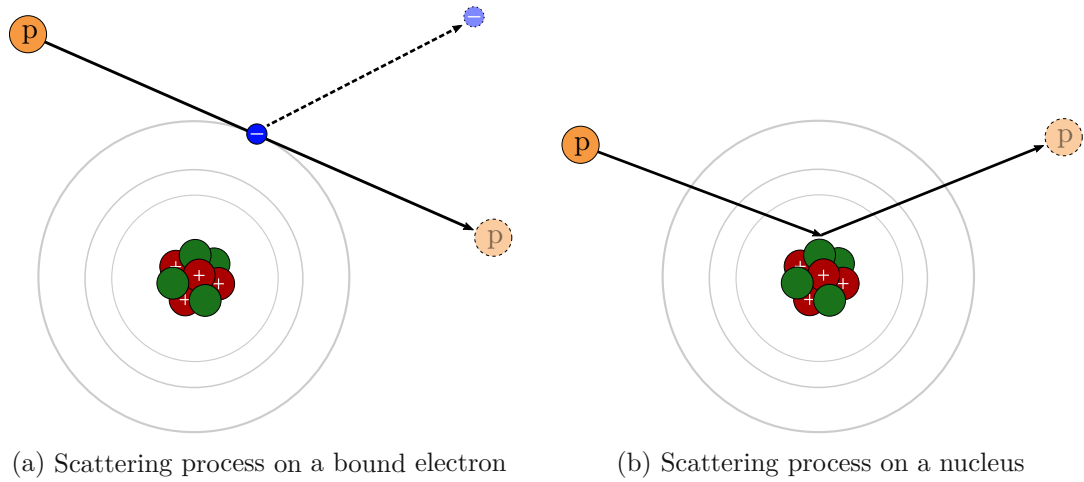


Figure 2.1: Particle scattering on atoms

2.1.2 Bremsstrahlung

The effect of bremsstrahlung occurs when charged particles are accelerated or decelerated, which leads to the emission of a photon. In matter this can happen through interaction with the coulomb field of the nuclei, like shown in Figure 2.2.

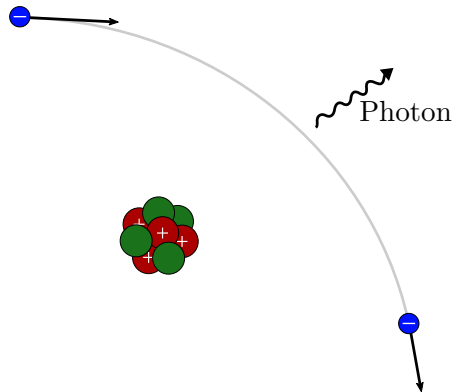


Figure 2.2: Emission of bremsstrahlung in matter

The amount of energy loss due to bremsstrahlung is inversely proportional to the mass squared and thus strongly pronounced for light particles and often negligible for heavy ions. Whether the loss is neglectable also depends on the particle energy. The critical energy for electrons, above which it can no longer be ignored, can roughly be given by [6]:

$$E_c \sim \frac{800}{Z} \text{MeV}, \quad (2.1)$$

where Z denotes the atomic number of the penetrated material. The critical energy for electrons is much smaller than the commonly used energies in high energy particle physics experiments, therefore the bremsstrahlung process is the most dominant in those

applications and for light ions other effects are often neglectable. This is contrary to the measurements done in this project with the electron emitter Strontium-90 (see Section 2.4.2).

2.1.3 Bethe-Bloch Formula

The Bethe-Bloch formula describes the average energy loss per length resulting from the inelastic collisions with bound electrons. For given material properties and a particle type, the equation gives the energy dissipated per path length depending on the particle velocity. The formula is given by [10]:

$$-\left\langle \frac{dE}{dx} \right\rangle = K \frac{Z}{A} \rho \frac{z^2}{\beta^2} \left[\frac{1}{2} \ln \frac{2m_e c^2 \beta^2 \gamma^2 T_{\max}}{I^2} - \beta^2 - \frac{\delta(\beta\gamma)}{2} - \frac{C(\beta\gamma, I)}{Z} \right], \quad (2.2)$$

where $K = 4\pi N_A r_e^2 m_e c^2$ and:

N_A	= Avogadro constant
r_e	= classical electron radius
m_e	= electron mass
c	= speed of light
Z	= atomic number of the absorbing material
A	= mass number of the absorbing material
I	= mean excitation potential of the absorbing material
z	= charge number of the particle
E	= energy of the particle
$\beta = v/c$	= relative particle velocity
γ	= Lorentz factor
T_{\max}	= maximal energy transfer in a single collision
x	= path length
C/Z	= shell correction
$\delta/2$	= correction for ultrarelativistic particles

At small non-relativistic velocities, the equation turns into a $1/v^2$ course. At very high relativistic velocities, a logarithmic dependence on $(\beta\gamma)^2$ can be observed, which leads to a slow relativistic increase.

The course of the Bethe-Bloch formula related to the density of different penetrated materials, dependent on different particle momentums can be seen in Figure 2.3. The courses for all materials show at around the same point $p = 3Mc$ a minimum. Particles with the corresponding momentum are also called MIP (minimal ionization particles). The comparison between the different curves indicates that the deposited energy per path length and density is about the same order of magnitude over the whole periodic table.

If the process is viewed from the perspective of the penetrated material, the stopping power of the material is obtained by:

$$S(E) = -\frac{dE}{dx}, \quad (2.3)$$

from which the Bragg curve can be derived. The Bragg curve describes the energy absorbed by the material per path length as function of the penetration depth. The exact curve appearance fluctuates, because of the stochastic nature of the interactions between matter and charged particles [12]. Figure 2.4 shows an average Bragg curve of silicon when interacting with an α particle of initial energy 5.486 MeV. It can be seen, that the particles lose more energy as their energies decrease, which is consistent with the Bethe-Bloch formula. The region around the maximum is known as the Bragg peak and has great importance in particle therapy (Section 2.2).

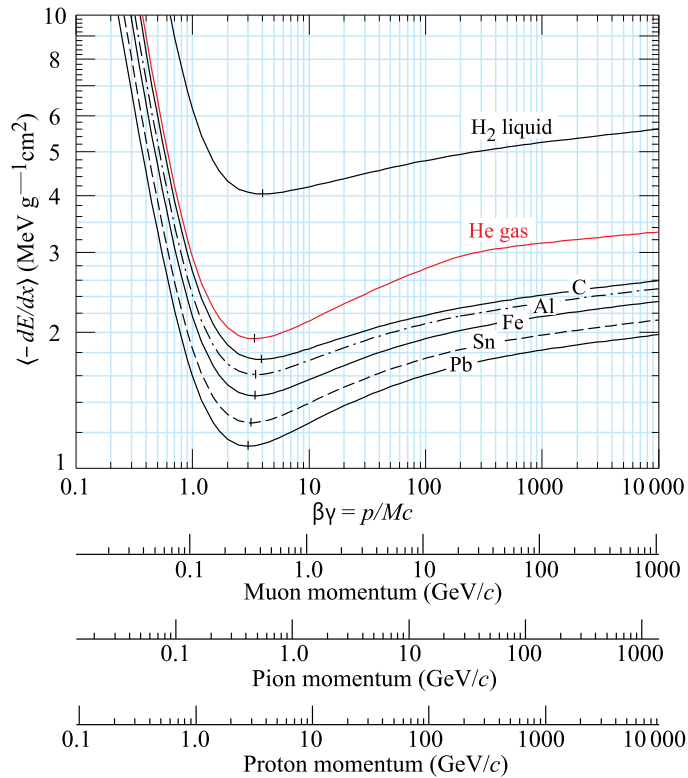


Figure 2.3: Mean energy loss per path length for different materials and different particles (Figure from [12])

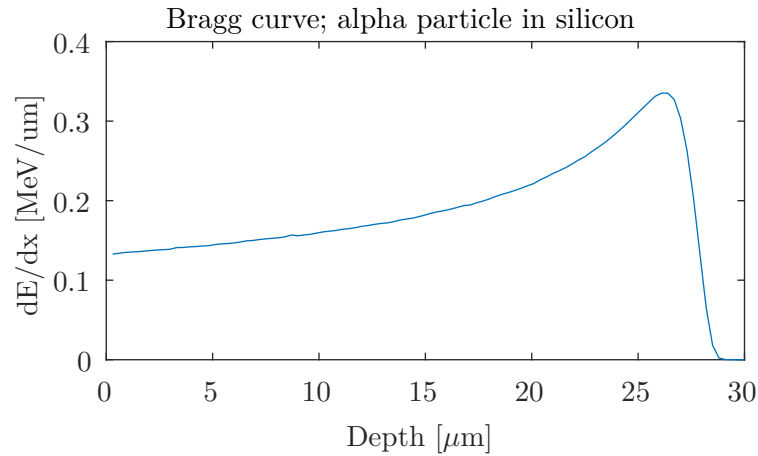


Figure 2.4: Shown is the averaged Bragg curve of silicon when interacting with α particles with an initial energy of 5.486 MeV. The graph was obtained from a simulation in SRIM [13], where the average was calculated from 2000 particles hits.

2.1.4 Stochastic fluctuation in the energy deposition

Although the Bethe-Bloch formula (2.2) can describe the average energy loss of particles in matter, it is not possible to predict the energy transfer in every specific interaction. This is due to the stochastic nature of the collisions. The thinner the penetrated material is, the greater is the influence of the fluctuations on the amount of the particle's total deposited energy. A factor κ introduced by Vavilov is used to describe the shape of the deposit energy distribution ($f(\Delta E)$) [10]:

$$\kappa = \xi/T_{max} \quad (2.4)$$

ξ is the prefactor of the logarithm in the Bethe-Bloch equation (2.2) multiplied by the material thickness Δx [10]:

$$\xi = \frac{1}{2} K \frac{Z}{A} \rho \frac{z^2}{\beta^2} \Delta x, \quad (2.5)$$

and T_{max} is the maximal transferred energy from the penetrating particle to an electron of the material after an interaction. For great κ values ($\kappa \gtrsim 1$) (thick material layers), the function f is a symmetric Gaussian distribution. For small κ values (thin material layers), the Gaussian goes over into a asymmetric Landau function (see Figure 2.5). A Landau function is build of a Gaussian central part and a tail up to infinity. The definition of the Landau is given by the integral [10]:

$$f_L(\lambda) = \frac{1}{\pi} \int_0^{\infty} \exp(-t \ln(t) - \lambda t) \sin(\pi t) dt \quad (2.6)$$

This standard form is then altered through scaling and translation to describe the deposited energy. Important parameters of the Landau distribution are the most probable value

(MPV), which is smaller than the mean value given by the Bethe-Bloch formula, and the full width of half maximum (FWHM) [10]:

$$W_{FWHM} = 4.018\xi \quad (2.7)$$

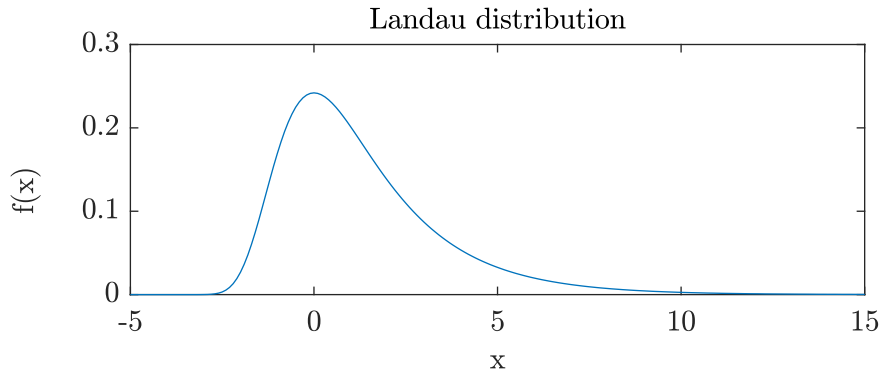


Figure 2.5: Example of a Landau distribution

2.2 Particle Therapy

In particle therapy, cancer patients are treated using protons or heavier particles such as carbon ions. The charged particles are used to destroy the DNA of tumor cells, thereby making the cells ineffective [1][2].

Figure 2.6 shows the comparison of the energy deposition of different particles in water. While the energy of protons and carbon ions can be chosen in such a way that the Bragg peak is precisely in the depth of the tumor, photons lose a considerable part of their energy already before that point. As a result, some tumors can be treated with protons in a more targeted manner than with photons, thus reducing the damage on healthy tissue [2].

2.2.1 Treatment plans

In particle therapies, so-called treatment plans are used. These plans specify the energy and position where the particles must penetrate the tissue to establish the Bragg peak at the position of the tumor. To create these plans, the surrounding tissue is first mapped by X-ray computer tomography. The results are the so-called Hounsfield values for all parts of the tissue. The Hounsfield scale indicates the normalized deviation of the photon attenuation of the material from that of water [14]:

$$HU = 1000 \cdot \frac{\mu - \mu_{water}}{\mu_{water}} \quad (2.8)$$

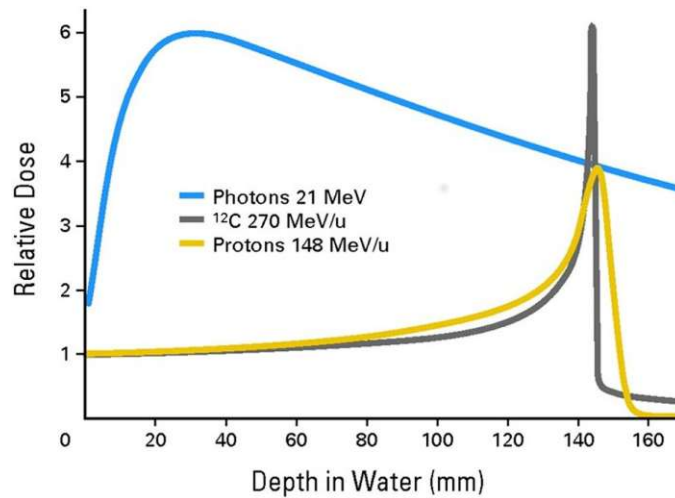


Figure 2.6: Bragg curve for different particles in water (Figure from [2])

With the Hounsfield values, an electron density is calculated, which can then be used to determine the stopping power for protons or heavier ions [15]. However, since photons interact differently with matter, deviations and errors occur. Due to these deviations, larger tolerance ranges must be considered, which can reduce the effectiveness of the treatment [16].

One way to bypass the conversion from photon attenuation to stopping power is the so-called proton computed tomography. Here, instead of X-rays, a proton beam is used to determine the stopping power properties. Concerning the pCT, one project has been carried out at the HEPHY in Vienna [17].

2.2.2 Intensities

In the treatments with ion beams, high intensities are necessary to treat patients in a reasonable time. In the MedAustron facility for example, medical intensities around 0.1 GHz to 1 GHz are used [3] (see Section 5.2). To ensure the safety of the patients at any time, the beam quality must be monitored before performing the treatment. This includes beneath others the determination of the particle rates and spatial distribution of the beam. Detectors used for that purpose are exposed to a heavy radiation load and must be chosen carefully to prevent wear of the detector material. Furthermore, if the particle beam is not only used for medical purposes but also for physical applications, much smaller particle rates are often needed, which requires additionally great flexibility of the detector system.

2.3 Semiconductor Detectors

In this project three types of sensors were mainly used: a silicon sensor, a silicon carbide, and a diamond sensor. All those detectors are semiconductors [18]; hence this chapter gives a brief introduction in how sensors based on semiconductors work. Detailed information of every sensor type can be found in the dedicated chapters (Silicon: Section 3.1; Silicon carbide: Section 3.3; Diamond: Section 3.2).

2.3.1 Function principle

Semiconductors are classified by their conductivity, which is typically between $1 \cdot 10^{-8} \text{ S/cm}$ - $1 \cdot 10^3 \text{ S/cm}$. They have near the absolute zero point a fully occupied valence band and an empty conduction band separated by a band gap. The gap is smaller than the one observed in insulator materials, which allows some electrons to reach the conduction band under thermal excitation easier, leading to a non-vanishing conductivity (Figure 2.7).[9]

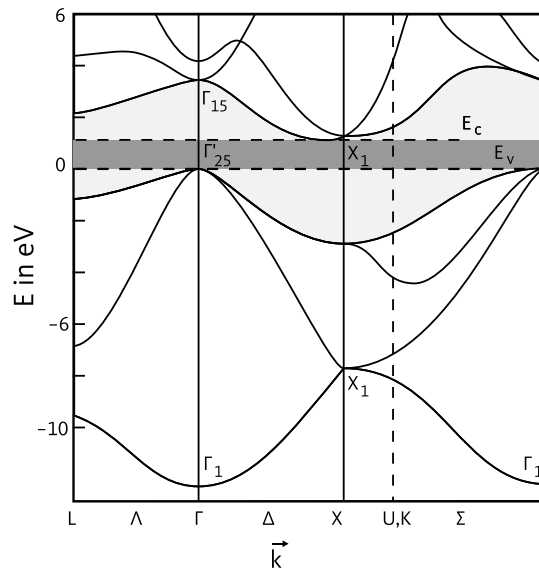


Figure 2.7: Shown is the band structure of silicon. The greyed-out area indicates the band gap, and E_c and E_v mark the edges of the conduction and valence band. (Based on [19] and adapted by [20])

In the so-called doping process, impurities are inserted into the crystal lattice of the semiconductor. A distinction is made between p-types and n-types. In p-types, atoms are implanted, which provide less electrons than the corresponding semiconductor atoms for the covalent bonds with the neighboring atoms. The results are additional energy states in the band gap near the valence band, which means that electrons from the valence band can more easily reach higher energy states during thermal excitation, leaving behind so-called holes. Those holes can be described as quasiparticles with a positive charge. In n-types, atoms are added, which have more electrons than needed for the covalent bonds

with the neighboring atoms. The additional electrons introduce new energy states close to the conduction band, and the electrons there can easily enter the conduction band upon thermal excitation.[9]

When a p-type and n-type semiconductor is brought together, the holes and electrons at the border diffuse into the opposite type and recombine with each other, leaving back a charge density of the contrary sign. As a result, a so-called depletion region, or junction region, is build up at the border between the two parts, in which, due to the potential difference, an electric field is established. This region forms a potential barrier for the charge carriers and prevents, after reaching a certain size, further diffusion. By contacting the two types at the opposite ends with a metallic conductor, a diode is made. Here the n/p-doped connection is also called the cathode/anode. If a positive voltage is applied to the anode, the charge carriers are forced to enter the depletion area and reduce thereby the charge difference in the zone. This leads to a lowering of the potential barrier (see third picture in Figure 2.8) and at some point, to a sharply increasing macroscopic current flow. The diode is operated in the forward direction. If, on the other hand, a negative voltage is applied, the holes and electrons are pulled towards the respective electrode, leading to a broadening of the depletion zone, like shown in the second picture of Figure 2.8. If the voltage is steadily increased, the depletion area spreads until the hole diode is depleted. The voltage, at which this is the case, is known as the full depletion voltage. In this reverse biasing, only a minimal dark current can flow through the potential.[9]

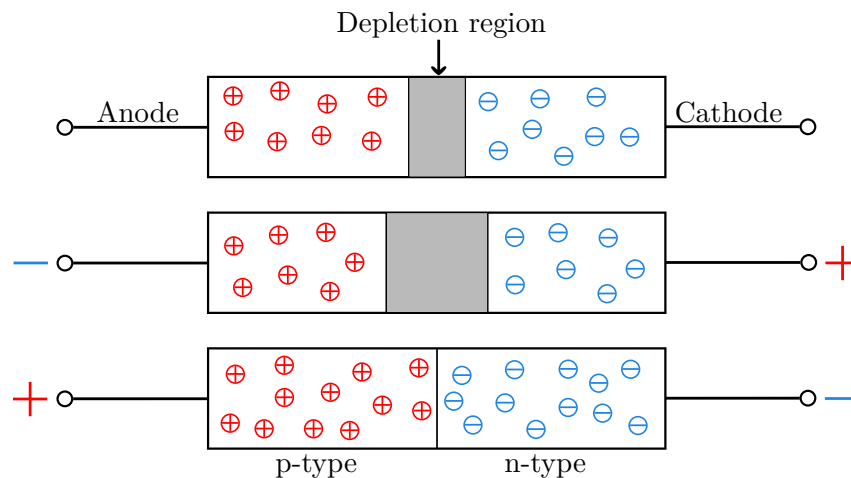


Figure 2.8: Different operation modes of a diode

If an ionizing particle hits the semiconductor in this state in the depletion zone, electron-hole pairs are generated and accelerated by the electric field in opposite directions:

$$\vec{F} = \vec{E}q \quad (2.9)$$

as shown in Figure 2.9. The drift of the charge carriers towards the electrical contacts generates a measurable current pulse, which can be used to detect the ionizing particle.[9]

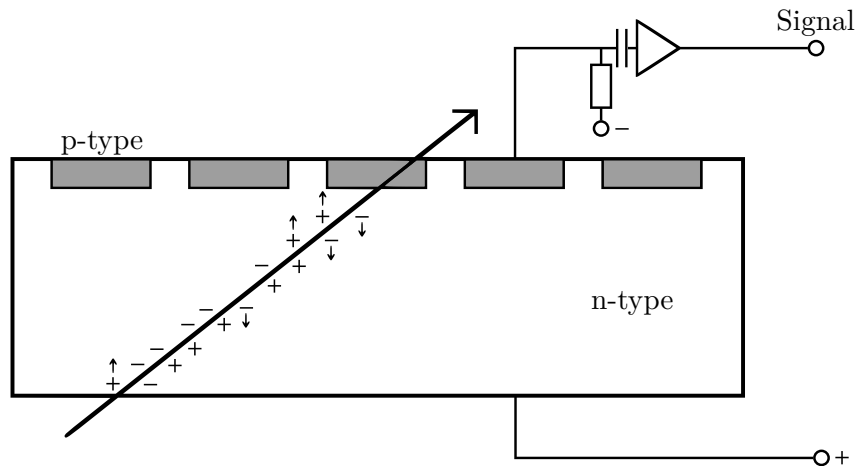


Figure 2.9: Schematic illustration of a doped semiconductor strip sensor

To obtain a spatial resolution, one of the two doped semiconductors can be formed in strips, like in Figure 2.9. Based on the different current pulses of the strips, it is possible to obtain information about the hit position in one coordinate. To get information in two coordinates, two of those detectors can be placed behind each other, rotated by an angle of 90° . Another possibility is to form the backside also in stripes, again orthogonal to the opposite surface, or by using substrate pixels, where each one is read out separately.[9]

The number of electron-hole pairs J generated by a particle is given by:

$$J = \Delta/P, \quad (2.10)$$

where P is the energy, which is necessary to generate an electron-hole pair. The energy depends on the detector material and is subject to stochastic fluctuations. Δ is the energy deposited in the detector by ionization, and as described in Section 2.1.3, is given by the Bethe-Bloch formula. Since the Bethe-Bloch equation only determines the average energy, the exact value is also a stochastic quantity. As a result, the generated number of charged pairs together with the signal height fluctuates stochastically. As explained in Section 2.1.4 the distribution follows for thin absorbers a Landau curve.

2.3.2 Charge carrier mobility

The motion of the charge carriers is described with the concept of mobility. The carrier mobility abstracts the change of motion due to different interactions in the solid and thus allowing it to give an expression for the average velocity of the carriers [21]:

$$\vec{v}_e = \mu_e \vec{E} \quad (2.11)$$

$$\vec{v}_h = \mu_h \vec{E}, \quad (2.12)$$

where μ denotes the mobility of the holes and electrons, \vec{v} their drift velocities and \vec{E} the electric field strength. The values of the mobilities depend on the material, the impurity

concentration, but also on the temperature and especially for high electric fields, also on the value of the field. The mobility can be derived from the Drude model, through which it is possible to calculate the averaged electron/hole movement \vec{v}_D in an electric field \vec{E} . [21]

$$m_{eff}(\dot{\vec{v}}_D + \frac{\vec{v}_D}{\tau}) = q\vec{E} \quad (2.13)$$

q is the charge of the hole $+e$ or electron $-e$, τ is the relaxation time and abstracts the different scattering processes in the lattice and m_{eff} is the effective masse, which includes the impact of the band curvature on the movement. The stationary solution of equation 2.13 is given by [21]:

$$\vec{v}_D = \frac{q\tau}{m_{eff}}\vec{E} = \mu\vec{E} \quad \Rightarrow \quad \mu_{e,h} = \frac{q\tau}{m_{eff}^{e,h}} \quad (2.14)$$

The mobilities of holes and electrons generally differ, and therefore they produce different current densities [21]:

$$\vec{J}_e = -en_e\mu_e\vec{E} \quad (2.15)$$

$$\vec{J}_h = en_h\mu_h\vec{E} \quad (2.16)$$

$$\vec{J} = \vec{J}_e + \vec{J}_h = e(n_h\mu_h - n_e\mu_e)\vec{E} = \sigma\vec{E}, \quad (2.17)$$

where σ is the electrical conductivity. From equations 2.15 - 2.17 it can be concluded that with larger mobilities, the signal currents become higher and thus also shorter for the same number of produced charge carriers. This also applies to an increasing of the electric field inside the sensor. [21]

2.3.3 Signal duration

A MIP particle penetrates through a full depleted planar semiconductor of the thickness d at time $t = 0$ and leaves behind a straight, uniformly distributed trail of N holes and electrons with a total charge of $\pm Ne$. The output current of the sensor, produced by the motion of the charge carriers, can be derived from equation 2.17, by replacing the spatial densities n_e/n_h with the line densities $-Ne/d/Ne/d$ and by assuming a homogenous electric field insight the detector with [22]:

$$i_e(t) = Ne\frac{v_e}{d}(1 - t\frac{v_e}{d}) \quad \text{for } 0 < t < \frac{d}{v_e} \quad (2.18)$$

$$i_e(t) = 0 \quad \text{otherwise} \quad (2.19)$$

$$i_h(t) = Ne\frac{v_h}{d}(1 - t\frac{v_h}{d}) \quad \text{for } 0 < t < \frac{d}{v_h} \quad (2.20)$$

$$i_h(t) = 0 \quad \text{otherwise} \quad (2.21)$$

The negative time proportional terms in the equations arise, because of the charge carries, which arrive at the electrodes and so no longer contribute to the total current. From the equations it can be concluded that the thinner the sensor, the shorter the output current impulse is.

A modification of the thickness leads also to a sensor capacitance change. A planar sensor diode can be modelled as a plate capacitor with the depletion zone as dielectric, whose capacitance can be calculated with:

$$C = \epsilon_0 \epsilon_r \frac{A}{d} \quad (2.22)$$

If the semiconductor has sufficiently high mobility, so that the motion of the charge carriers towards the metallic contacts can be neglected and if an electrical circuit with input resistance R_e is connected to the detector, the sensor discharges a charge Q , produced by a particle at time $t = 0$, via a current $I(t)$:

$$I(t) = I_0 \exp\left(-\frac{t}{\tau}\right) \quad \tau = R_e C \quad (2.23)$$

It follows that the higher the input resistance and the thinner the detector, the longer and smaller the generated current pulse.

Consequently, both the mobilities and the thickness can influence the signal duration. The duration of the output signal is an important property of a detector system, because longer signal durations lead to pile-up effects at lower particle intensities and therefore reduces the range of possible operation settings.

2.3.4 Pile-up effect

When two particles hit a semiconductor detector simultaneously, the produced number of electron-hole pairs adds up and the sensor behaves as if one particle had deposited the combined energy in the detector. This situation is called the pile-up effect and is visualized graphically in Figure 2.10 [23]. In each case, two particles hit the sensor with different time delays. While in the first diagram, it is still possible to distinguish between the two hits (for example with a threshold discriminator at the half of the signal amplitude), this is no longer the case in the third graph. Due to the Landau fluctuation of the output signal (Section 2.3.1), it is not possible to use the signal height to determine exactly how many particles have hit the detector. Therefore, the signal duration limits the time that must pass between two particle hits in order to distinguish them.

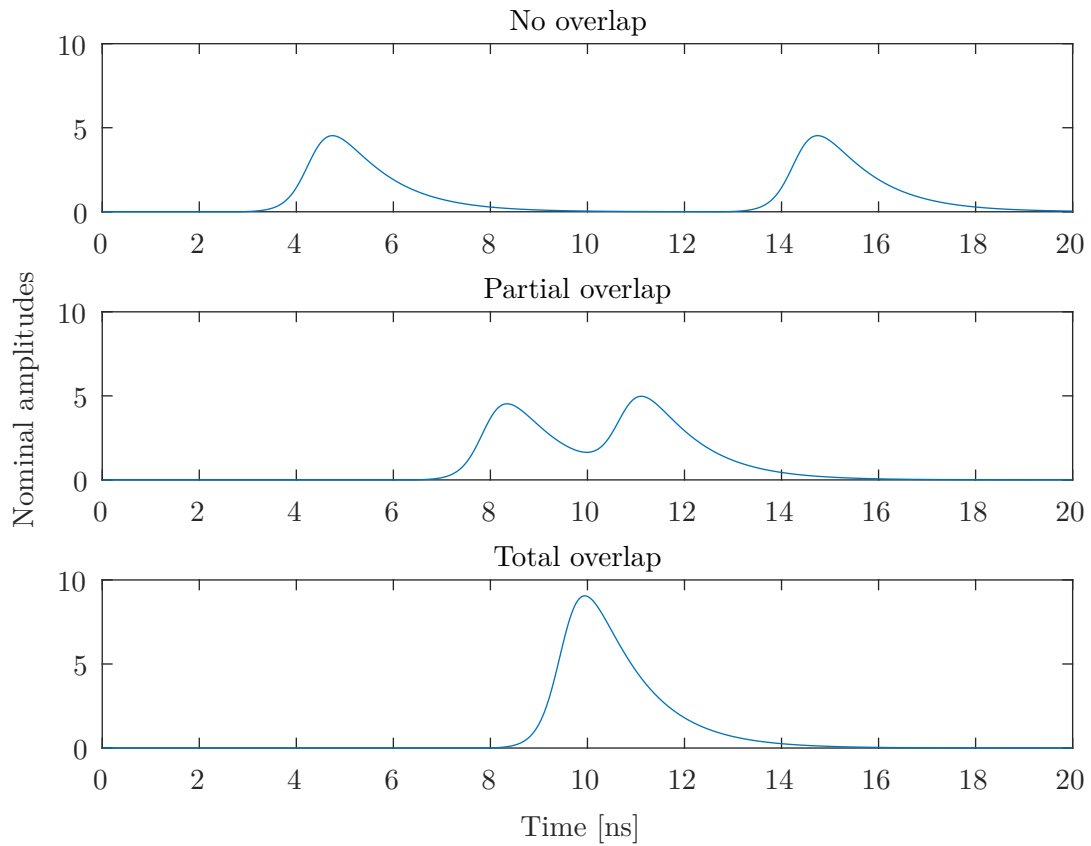


Figure 2.10: Shown is a schematic illustration of the pile-up effect like it could be seen at the output of a transimpedance sensor readout system.

2.4 Radioactive sources

Radioactive materials make it possible to carry out fundamental detector tests without a particle accelerator. Of particular interest are sources that create MIP-like signals, which are used to estimate the minimal signal levels, and sources that emit particles with uniform energies, allowing a characterization of the whole detector system. For each of these purposes, a separate radioactive source was chosen. These are the β^- emitter Strontium-90 and the α emitter Americium-241 shown in Figure 2.11.



Figure 2.11: The radioactive sources used in this project

2.4.1 Americium-241

In α decays a ${}^4\text{He}$ nuclide is emitted from the parent nuclide (Figure 2.12). The gain in kinetic energy E after the decay can be calculated from the mass defect [24]:

$$E = \Delta mc^2 \quad \Delta m = m_P - m_D - m_\alpha, \quad (2.24)$$

where m_α , m_D and m_P are the masses of the α particle, the daughter nuclide and the parent nuclide. The kinetic energy distribution between the daughter nuclide and the α particle is uniquely determined by the momentum conservation and depends on their mass relation [24]:

$$E_D = \frac{m_\alpha}{m_D} E_\alpha \quad (2.25)$$

As a result, the emitted α particles have a discrete number of energy values (they are mono-energetic). This mono-energetic spectrum makes it possible to characterize detector systems so that the amount of energy deposited in the sensor can be directly assigned to a specific height of the output signal, which is done by measuring the output signal produced by the mono-energetic particles. In some decays it can happen that the daughter nuclide is left in an excited state. The nuclide can enter then the ground state again by an emission of a gamma photon [24]. Americium-241 has a half-life of 432.6 years and decays in most cases under the release of an α particle with an energy of 5.486 MeV (Figure 2.13) [25]. The used Americium source had an activity of 9.5 kBq at the time of its acquisition in 2018 and is therefore not subject to any legal restrictions in Austria, which makes handling while performing tests easier. Due to the long half-life, it can be assumed that the activity has hardly changed til today.

According to the discussion in Section 2.1.3, an α particle must have at least an approximately energy of:

$$p_{\alpha MIP} = 3m_\alpha c \quad \Rightarrow \quad E_{\alpha MIP} = \sqrt{10}m_\alpha c^2 = 11.79 \text{ GeV} \quad (2.26)$$

to show MIP like behavior. By comparing the value to the possible alpha energies in Figure 2.13, it can be concluded that no MIP behavior can be expected.

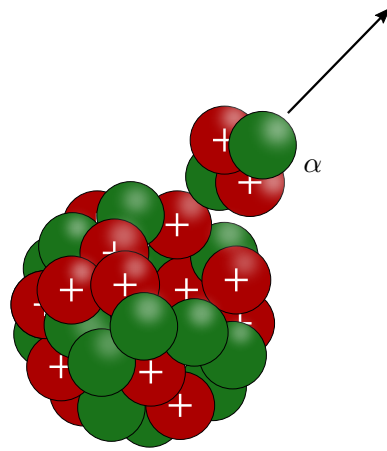


Figure 2.12: Schematic illustration of the α decay

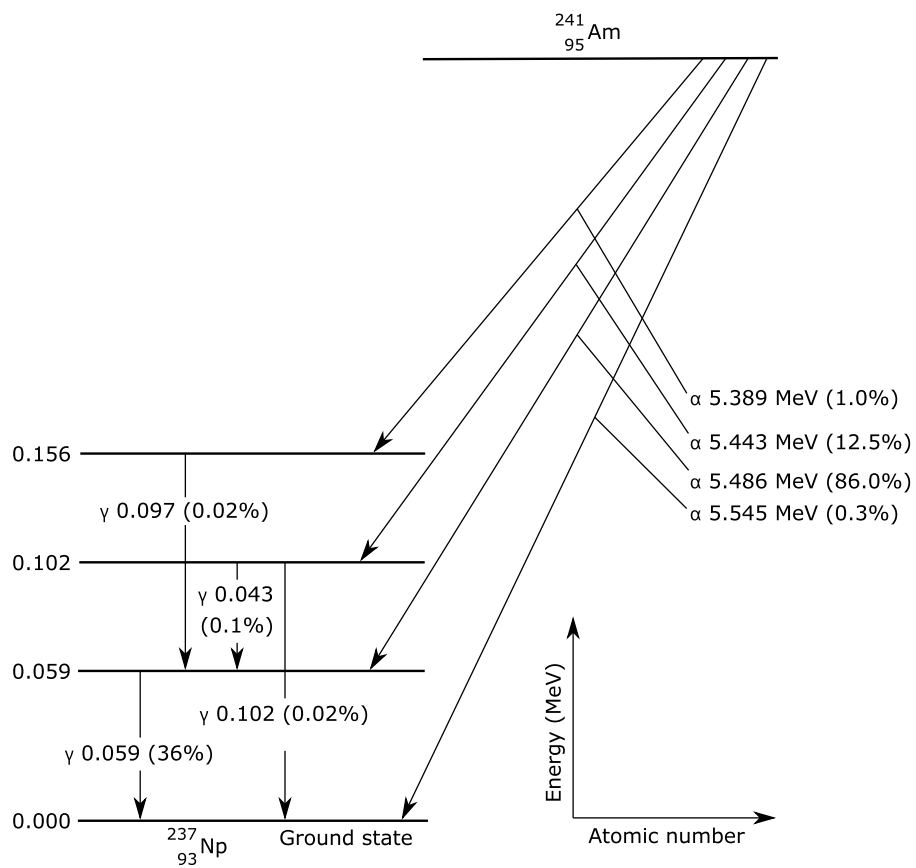


Figure 2.13: Radioactive decay scheme of Americium-241 (Based on [24])

As shown in Figure 2.4, an α particle with an energy of 5.486 MeV dissipates its whole energy in the first 30 μm of a silicon sensor. As comparison, a proton MIP particle with 2.5 GeV, which has an energy loss of 3.868 MeV/cm in silicon [26] (density: 2.329 g/cm³ [27]), dissipates an energy of:

$$3.868 \text{ MeV/cm} \cdot 190 \cdot 10^{-4} \text{ cm} = 73.49 \text{ keV}, \quad (2.27)$$

in a 190 μm detector (thickness of the silicon sensor used in this project), which is a fraction of the energy dissipated by the α particle. In the calculation, it was assumed that the total proton energy is only slightly changed while passing through the sensor. In addition it must be noticed, that the energies from Figure 2.13 only specify the α particle energy right after the decay. But the α particle lose already some of its energy while travelling through the Americium material and in the air between source and sensor. The effects of the interactions in the air were determined in the bachelor thesis [28]. The result is given in Figure 2.14. It shows that the original discrete energy values become continuously distributed. This has the consequence that the output signals cannot be assigned unanimously to an energy deposition in the sensor, limiting so the accuracy of the detector system characterization.

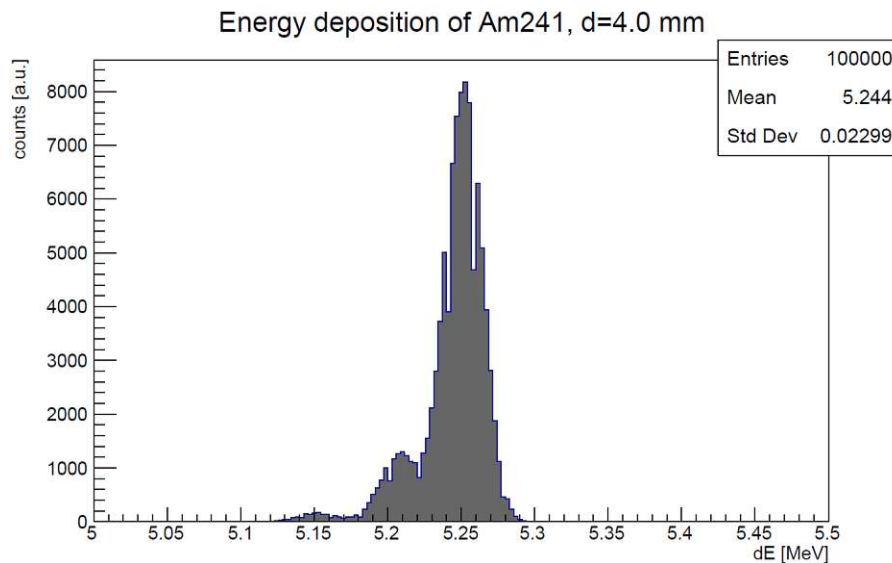


Figure 2.14: Shown is the energy spectrum of Am-241 particles in 4 mm distance to the source. (Kindly provided by [28])

Due to the non MIP behavior of the α particles, the Americium source can not be used to operate the sensor systems at their minimal signal heights. Nevertheless, because of the simple handling, which allows to analyze effects of changes concerning the detector system faster, and the possibility to characterize the detector systems, even if the accuracy is limited, the source was used. Additionally, the high signal amplitudes can give an

impression of the detector system behavior at low particle energies and allow to operate the system without the influence of a second amplifier like that one used in combination with the Strontium source in the measurements of Section 5.1.2.

2.4.2 Strontium-90

In the β^- decay a neutron decays in a proton, an antineutrino, and an electron (Figure 2.15). While the proton is bound on the daughter nuclide, the other two particles are emitted. Therefore, the released electron is also called β^- particle. The gain in kinetic energy is divided among three participants. In contrast to the α decay, the conservation of momentum determines the β^- particle's kinetic energy not unique, which leads to a continuous distribution of the energy [29]. This distribution characterizes a specific radionuclide. The full energy spectrum of a Strontium-90 source, like in Figure 2.16 is a combination of energies from the daughter nuclide Yttrium-90 and the Strontium decay itself [30].

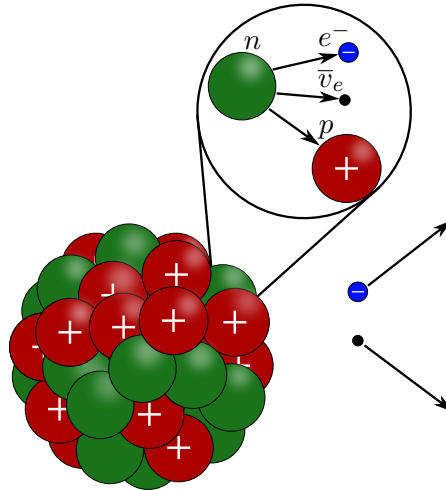


Figure 2.15: Schematic illustration of the β^- decay

Figure 2.18 shows the electron stopping power due to collisions and bremsstrahlung radiation of silicon (data from [26]) (density: 2.329 g/cm^3 [27]). It can be concluded that the minimal ionization energy is 1.25 MeV and the radiation energy loss can roughly be neglected for all energies of the Sr-90 spectrum (Figure 2.16). Electrons with an energy between 0.9 MeV and 2.5 MeV all have nearly the same energy deposition and therefore all show MIP like behavior. This range corresponds to the upper part of the Sr-90 energy spectrum. From Figure 2.18 it can be seen that MIP electrons lose 3.494 MeV/cm in silicon through collisions. Therefore an energy deposition in a $190 \mu\text{m}$ silicon detector of:

$$3.494 \text{ MeV/cm} \cdot 190 \cdot 10^{-4} \text{ cm} = 66.39 \text{ keV} \quad (2.28)$$

can be determined, which is nearly the same as the energy loss of the proton MIP calculated in equation 2.27.

In the bachelor thesis [28], it was shown that particles with energies below 0.8 MeV from the Strontium-90 spectrum are strongly suppressed after the penetration of a PCB board with 1.60 mm thickness (Figure 2.17). Thus, it can be assumed that most of the particles detected after such a PCB board had enough energy at the time of their emission to be considered as MIP. In the measurement setup of Section 5.1.2 the particles must penetrate through two PCB boards, which even increases the filtering effect.

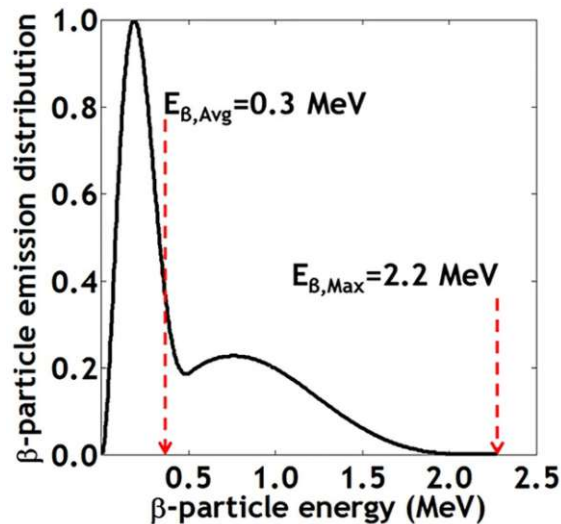


Figure 2.16: Strontium-90 energy spectrum (Figure from [30])

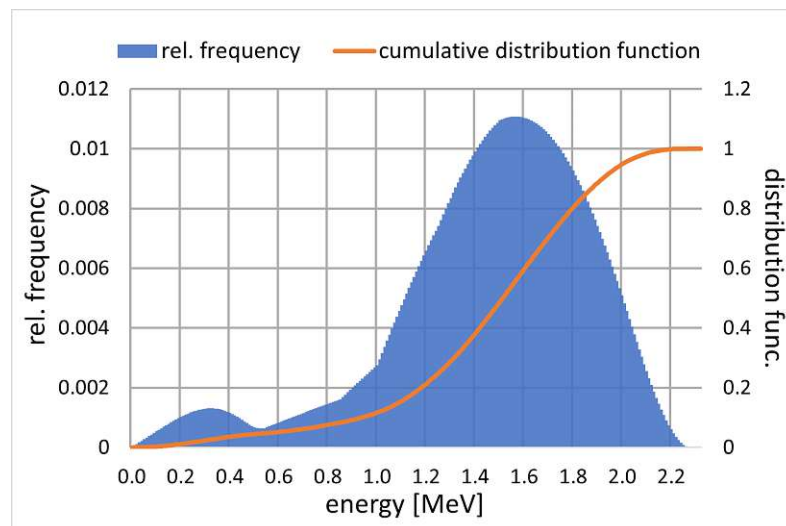


Figure 2.17: Shown is the energy spectrum of Strontium-90 particles after they have travelled through a PCB board with 1.60 mm thickness. (Kindly provided by [28])

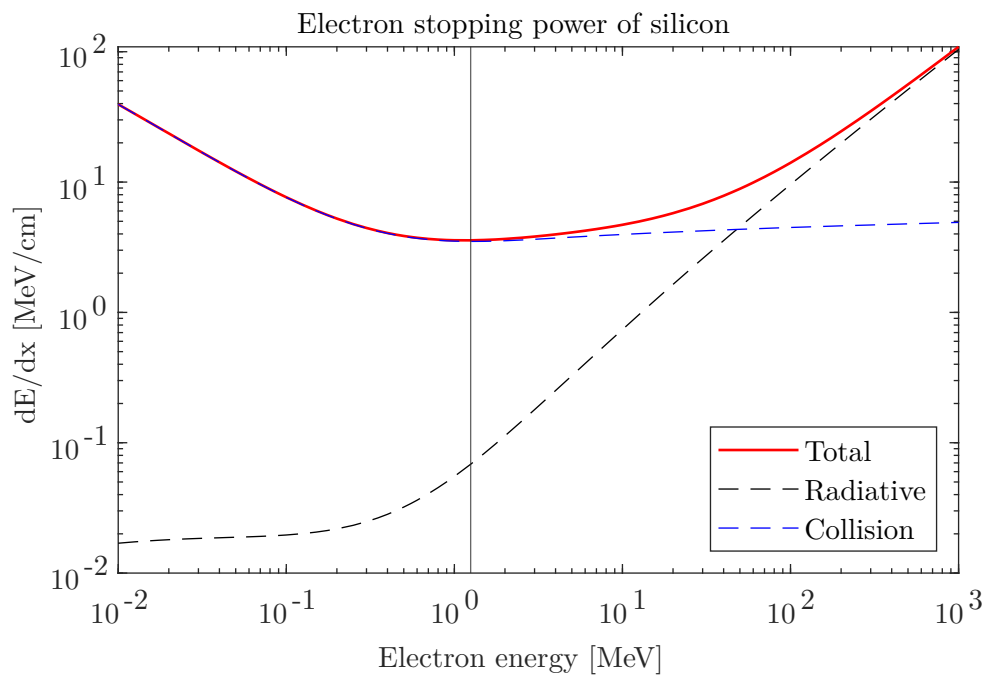


Figure 2.18: Electron stopping power in silicon [26]. The vertical line marks the minimal ionization energy 1.25 MeV.

3 Solid state sensors

The planar silicon carbide sensor of Section 3.3 plays a leading role in this project, but to compare the attributes of the sensor material to other semiconductors in a similar environment, some experiments, conducted with the silicon carbide detector, were also carried out for a silicon (Section 3.1) and a diamond (Section 3.2) sensor. Furthermore, an LGAD (low gain avalanche detector) was used to produce a trigger signal in the beta telescope setup of Section 5.1.2.

This chapter presents first the general properties of the corresponding detector materials and then specific features of the sensors. To do so, characterization measurements (Section 3.5) in the form of current-voltage and capacitance-voltage measurements were conducted. Additionally, results from sensor simulations done in a program called Weightfield2 are shown (Section 3.6.1).

3.1 Silicon sensor

Silicon is an indirect semiconductor and has a bandgap at room temperature of 1.1 eV [4], which is smaller than the one of diamond and silicon carbide. It requires an average energy of 3.6 eV [31] to create a single electron-hole pair. Silicon crystallizes in a diamond cubic lattice, in which each silicon atom is connected by covalent bonds to four neighboring atoms.

From thermal excitation, pure silicon contains about $1.01 \cdot 10^{10}$ electron-hole pairs per cm^3 at room temperature ($T=300\text{ K}$) [9]. Therefore, a sensor with a thickness and area of $190\ \mu\text{m}$, $25\ \text{mm}^2$ holds a total number of $4.8 \cdot 10^7$ e/h pairs. A MIP proton, on the other hand, produces about $2 \cdot 10^4$ e/h pairs in a sensor of the same size, which leads to an unacceptable signal-to-noise ratio (SNR) at room temperature. Therefore, unlike diamond, intrinsic silicon is not used directly as a sensor. The density of the free charge carriers must be reduced to improve the SNR, which can be done by combining opposite doped silicon in one sensor as described in Section 2.3. The same also applies to sensors made of silicon carbide.

The silicon sensor used in this project (Figure 3.1) is a n-on-p doped planar single-channel diode from Infineon. Thus, the sensor bulk consists of p-doped and the substrate of n-doped silicon. The sensor's thickness and area is $189\ \mu\text{m}$ and $5\ \text{mm} \times 5\ \text{mm}$. The detector is contacted via an aluminum layer in which an optical hole is placed in the center. The ring around the sensor forms the contact to a Guard Ring.

From the measurements of the next section (Figure 3.8 and Figure 3.9), the sensor capacitance and dark current values for the operating voltages 100 V, 200 V and 400 V can be determined:

Bias voltage [V]	Dark current [nA]	Capacitance [pF]
100	260	15
200	260	14.9
400	280	14.9

Table 3.1: The dark current and capacitance values of the silicon diode for different bias voltages

In addition, a diode full depletion voltage of 44.1 V can be obtained from Figure 3.9. With the full depletion voltage and sensor thickness, it is possible to calculate other detector quantities at room temperature [32]:

Doping concentration:	$1.59 \cdot 10^{12} / \text{cm}^3$
Resistivity:	$8.2 \text{ k}\Omega \text{ cm}$
p-Mobility:	$477 \text{ cm}^2 / (\text{V s})$

Table 3.2: Different characteristics of the planar silicon diode

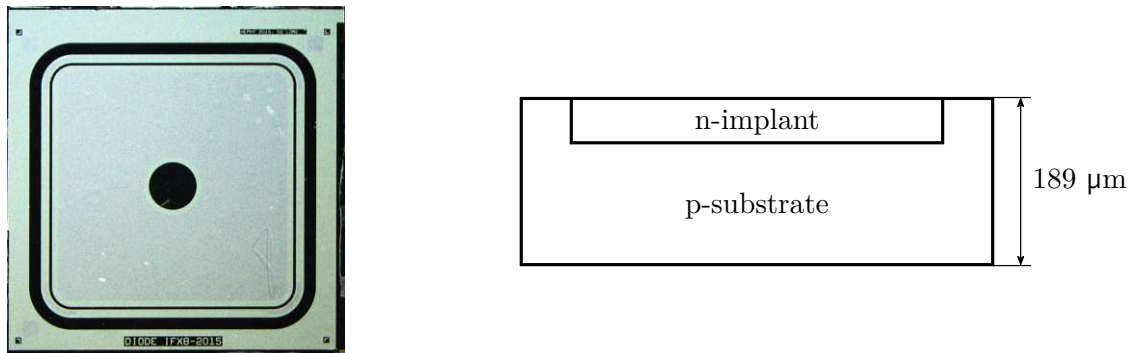


Figure 3.1: Shown is a picture and a schematic illustration of the cross-section of the planar n-on-p silicon diode used in this project.

3.2 Diamond sensor

Diamond has a bandgap of approx. 5.5 eV [33] and an energy of approx. 12.86 eV [34] is needed to create a charge pair, which means that electrons are less likely to be lifted into the conduction band by thermal excitation than in silicon, resulting in a lower free charge carrier density. Consequently, diamond sensors do not need to be doped, no space charge region needs to be created, they can be used directly as detector and, unlike the other sensors in this project, they can be operated in both current directions. The larger bandgap also leads to a reduction of the dark current and thus reducing cooling requirements. In addition, diamond has at least a three times higher radiation hardness than silicon [35] and is able to collect created charges not less than two times quicker [36]. Disadvantages are that the area of diamond detectors is limited to a square of a few cm² and that the acquisition costs are very high due to the small number of suppliers.

The sensor used in this project consists of a CVD diamond. CVD diamonds are grown artificially using the chemical vapor deposition (CVD) process. Due to this manufacturing process, grain boundaries are formed in the polycrystalline crystal, which can serve as charge traps and introduce energy states within the bandgap [37]. This reduces the mean charge carrier lifetimes τ of the holes and electrons, with which an average charge collection distance d_c is associated:

$$d_c = v_e \tau_e + v_h \tau_h \quad (3.1)$$

The electrons and holes can only contribute to the output signal while they are traveling through the sensor (see Section 2.3.3). The maximum distance is limited by the thickness of the detector. Therefore, if the charge collection distance is small compared to the detector thickness, a smaller collection distance means also a smaller sensor efficiency. The total charge of the electrons holes, which reach the electrons in a detector with thickness d , after a charge generation of Q_p , can be approximated with:

$$Q_c \approx Q_p \frac{d_c}{d} \quad (3.2)$$

and thus a charge collection efficiency *cce* of:

$$cce = \frac{Q_c}{Q_p} \approx \frac{d_c}{d} \quad (3.3)$$

can be estimated. A diamond sensor can be "pumped" before a measurement to maximize the collection efficiency. In this procedure, the detector is exposed to particle radiation for a specific time so that the traps are constantly filled and thus no longer serve as charge carrier traps. The process can be reversed by exposing the sensor to ultraviolet light. Thereby, the traps are emptied again, and the diamond can be found again in its "unpumped" form.[38][39]

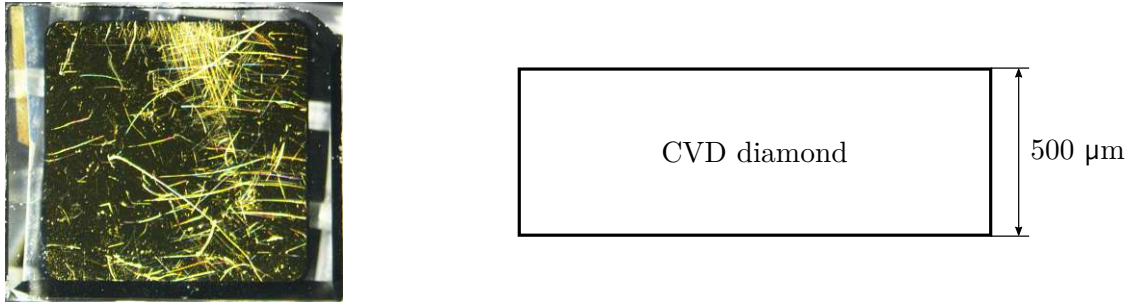


Figure 3.2: Shown is a picture and a schematic illustration of the cross-section of the planar CVD diamond used in this project. The surface of the electrical contact is heavily scratched, but this does not influence the sensor's functionality.

The CVD diamond sensor (Figure 3.2) of this project, which was provided by the company Cividec, has an area of $4\text{ mm} \times 4\text{ mm}$ and a thickness of $500\text{ }\mu\text{m}$. As can be seen in the results of the CV measurements (Figure 3.9), the capacitance value of the diamond sensor nearly not change in the voltage range 0 V to 950 V , resulting from a non-existing growing depletion region. The following table summarizes the capacitance and dark current values for certain bias voltages:

Bias voltage [V]	Dark current [pA]	Capacitance [pF]
100	< 0.09	2.29
200	< 0.09	2.28
400	0.26	2.28

Table 3.3: The dark current and capacitance values of the CVD diamond sensor for different bias voltages

3.3 Silicon carbide

Silicon carbide sensors consist of carbon-silicon compounds that join together in a tetrahedral arrangement in which four carbon atoms surround a silicon atom in the center. They can crystallize together in various crystal structures. These are all polytypes, in which the sequence and orientation of crystal layers may change along one direction, but the composition of every layer remains the same. It is possible to describe the lattices of polytypes as a close-packing of equal spheres structure. The layers in such structures can be stacked in different sequences. After the first layer A is fixed, there are two possibilities for the next layer B to be placed on top of A. The third layer can then either be arranged in the same position as the first layer A or snap into a third, new position C. For each additional layer, two different positions are possible. The technologically most important stacking sequences of silicon carbide are named as 3C-SiC, 4H-SiC and 6H-SiC. The letter H/C stands for a hexagonal/cubic structure formation. The number in front of the letter

indicates the number of layers after the sequence repeats itself.[40]

In general the properties of the various crystal structures differ, so also the height of the bandgap, which are given in Table 3.4 for the structures 3C-SiC, 4H-SiC and 6H-SiC. It can be seen that all bandgaps lie between that of silicon and diamond. In comparison to silicon, this leads to a reduction of the dark current, which eliminates the need for cooling even in harsh environments. In addition silicon carbide is characterized by its fast signals due to the high electron mobility and a temperature independent performance up to few 100 °C [41]. One of the most important property for this project is the enhanced radiation hardness [5], compared to silicon detectors and scintillators, which leads to fewer material alterations, resulting in a longer lifetime, especially under high radiation conditions.

Lattice structure	Bandgap height [eV]
3C-SiC:	2.40
4H-SiC:	3.26
6H-SiC:	3.02

Table 3.4: The heights of the bandgap for different silicon carbide lattice structures [42]

The silicon carbide sensor of Figure 3.3, which was used in this project and provided by CNM (National Microelectronics Center) Barcelona, is a 4H crystal grown epitaxially on a wafer. The area of the p-on-n doped diode is 3 mm × 3 mm, and it has a thickness of 435 μm, of which 45 μm belong to the active region and can be depleted. The p-substrate is contacted using bonding wires via the four pads on top, while the n-bulk is connected to the bottom side surface. The necessary charge pair creation energy in such a 4H-SiC sensor is not fully clear. Values starting from 5.05 eV [43] up to 8.6 eV [44] have been already reported. The value used in this project is 7.28 eV [45], which is one of the most recently published values. The full depletion voltage V , which is determined from Figure 3.9 to be 296 V, the resistivity ρ , which is given by the manufacturer (20 Ω cm), and the thickness of the active region W can be used in the following formula to calculate the doping concentration N and the electron mobility μ [46]:

$$\rho = \frac{1}{e\mu N} \Rightarrow \mu = \frac{1}{e\rho N} \quad (3.4)$$

$$W \approx \sqrt{2\epsilon_0\epsilon_r\mu\rho V} \Rightarrow N \approx \frac{2\epsilon_0\epsilon_r V}{eW^2} \quad (3.5)$$

The resulting values are summarized in the following table:

Doping concentration:	$1.561 \cdot 10^{14}/\text{cm}^3$
Resistivity:	$20 \Omega \text{ cm}$
n-Mobility:	$2000 \text{ cm}^2/(\text{V s})$

Table 3.5: Different characteristics of the silicon carbide diode

From the results in Figure 3.8 and Figure 3.9 the dark current and sensor capacitance for the operating bias voltages of Section 5 can be given:

Bias voltage [V]	Dark current [pA]	Capacitance [pF]
100	6.6	32.5
200	3.7	24
400	2.3	19.3

Table 3.6: The dark current and capacitance values of the silicon carbide sensor for different bias voltages

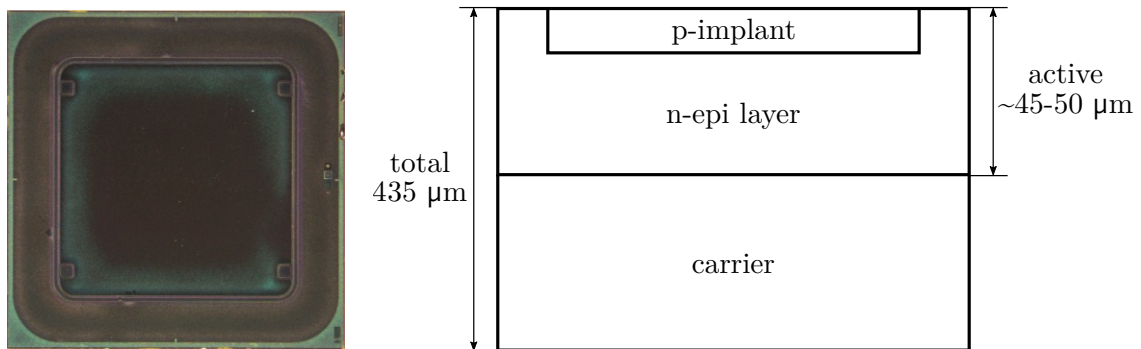


Figure 3.3: Shown is a picture and a schematic illustration of the cross-section of the planar p-on-n silicon carbide epitaxial diode used in this project.

3.4 LGAD sensor

Low gain avalanche detectors are doped silicon sensors with an extra gain layer for signal amplification. Figure 3.4 shows the operating principle of a LGAD sensor using an n-on-p diode. Just below the n+ doped top layer, a moderately p-doped layer is added, which is called multiplication layer. Between this p-doped layer and the n+ layer, a strongly increased electric field is formed, which gives the charge carriers drifting to the cathode enough energy to ionize other electrons and thereby multiplying the number of e/h-pairs.

The rate G at which electron-hole pairs are generated depends on the ionization rates α_e , α_h and the electron, hole densities n_e , n_h and is given by:

$$G = \alpha_e v_e n_e + \alpha_h v_h n_h \quad (3.6)$$

α_e and α_h in turn depend on the electric field strength E in the multiplication layer:

$$\alpha = \frac{E}{E_{th}} \exp\left(\frac{-E_i}{E}\right), \quad (3.7)$$

where E_i is the minimal electric field strength necessary for an avalanche charge carrier production and E_{th} the ionization energy necessary to create an electron hole pair. The electric field strength is proportional to the square root of the p doping density and the applied bias voltage. Typical values for the electric field are around 300 kV/cm, with a gain factor of 10.[47]

In this project, a n-on-p LGAD sensor (Figure 3.5) from FBK (Fondazione Bruno Kessler) was used. The active zone has an area and thickness of $2\text{ mm} \times 2\text{ mm}$ and $50\text{ }\mu\text{m}$. The output signal gain is 10.

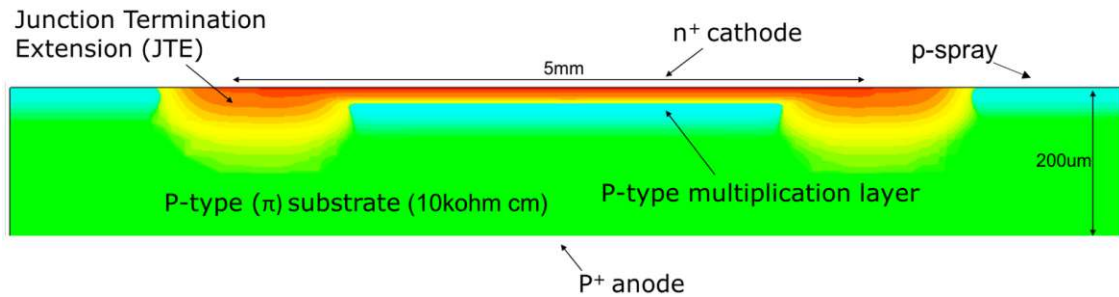


Figure 3.4: Shown is the structure of a planar LGAD sensor based on a silicon n-on-p diode. (Figure from [47])

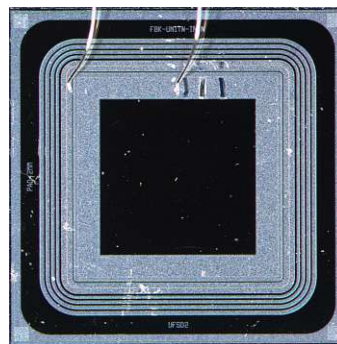


Figure 3.5: Shown is the n-on-p LGAD sensor, which is used in the beta telescope measurements of Section 5.1.2. The wires connecting the sensor to the UCSC readout circuit (see Section 4.1) can also be seen.

3.5 Characterization measurements

To characterize the presented sensors, two fundamental measurements were carried out.

The first one is a current-voltage relation measurement, here is the bias voltage increased in defined steps, while the sensor current is measured. Figure 3.6 shows the corresponding measurement setup, including the following devices:

- Electrometer Keithley 6514
- Source measure unit (SMU) Keithley 237

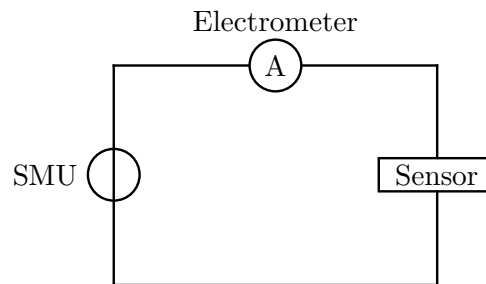


Figure 3.6: Shown is the IV measurement setup. While the SMU increases the sensor bias voltage, the electrometer measures the resulting current flow.

The results are the dark current values of each detector (Figure 3.8).

In the second one, the sensor capacitances are measured for different bias voltages. The result is then used to determine the full depletion voltages. The corresponding measurement setup (Figure 3.7) includes the following devices:

- LCR meter Agilent 4284A
- Source measure unit (SMU) Keithley 237

In addition, a decoupling box is deployed. The box consists of high voltage capacitors, which separate the DC-bias voltage from the AC-LCR measurement voltage. After that, the LCR-meter measures the phase shift between the AC voltage and the AC current to determine the sensor capacitance.

As discussed in Section 2.3, the depletion zone expands with an increasing inverse bias voltage, which leads to a decreasing sensor capacitance. The thickness of the depletion region is proportional to $d \propto \sqrt{V}$, and the planar sensors can be modeled as plate capacitance $C = \epsilon A/d$. Consequently, a relation between bias voltage and sensor capacitance of $1/C^2 \propto V$ can be found. The relation is fulfilled until the hole sensor is depleted and the junction region can not expand further. By plotting $1/C^2$ over the bias voltage (Figure 3.9 right side), the full depletion voltage can be found at the intersection point of a line, won from a linear interpolation of the first measurement points, and the final $1/C^2$ value. The result is the full depletion voltage for the silicon (44.1 V) and for the silicon carbide detector (296 V).

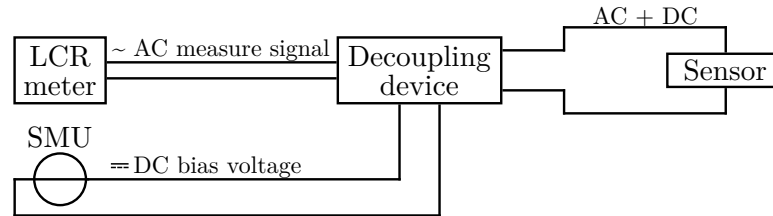


Figure 3.7: Shown is the CV measurement setup. The SMU increases the bias voltage and the LCR meter measures the corresponding sensor capacitances. LCR meter and the DC bias voltage of the SMU.

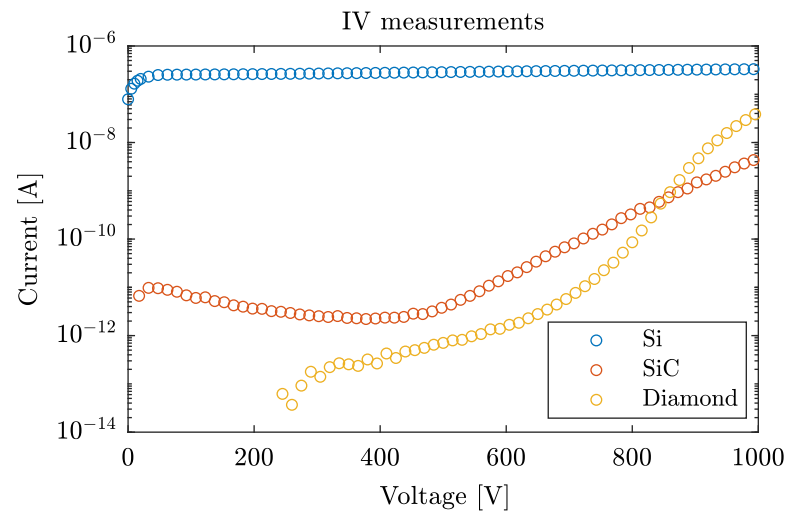


Figure 3.8: Shown are the sensor currents, measured with the electrometer in Figure 3.6, for different bias voltages and for all three sensors silicon, silicon carbide and diamond.

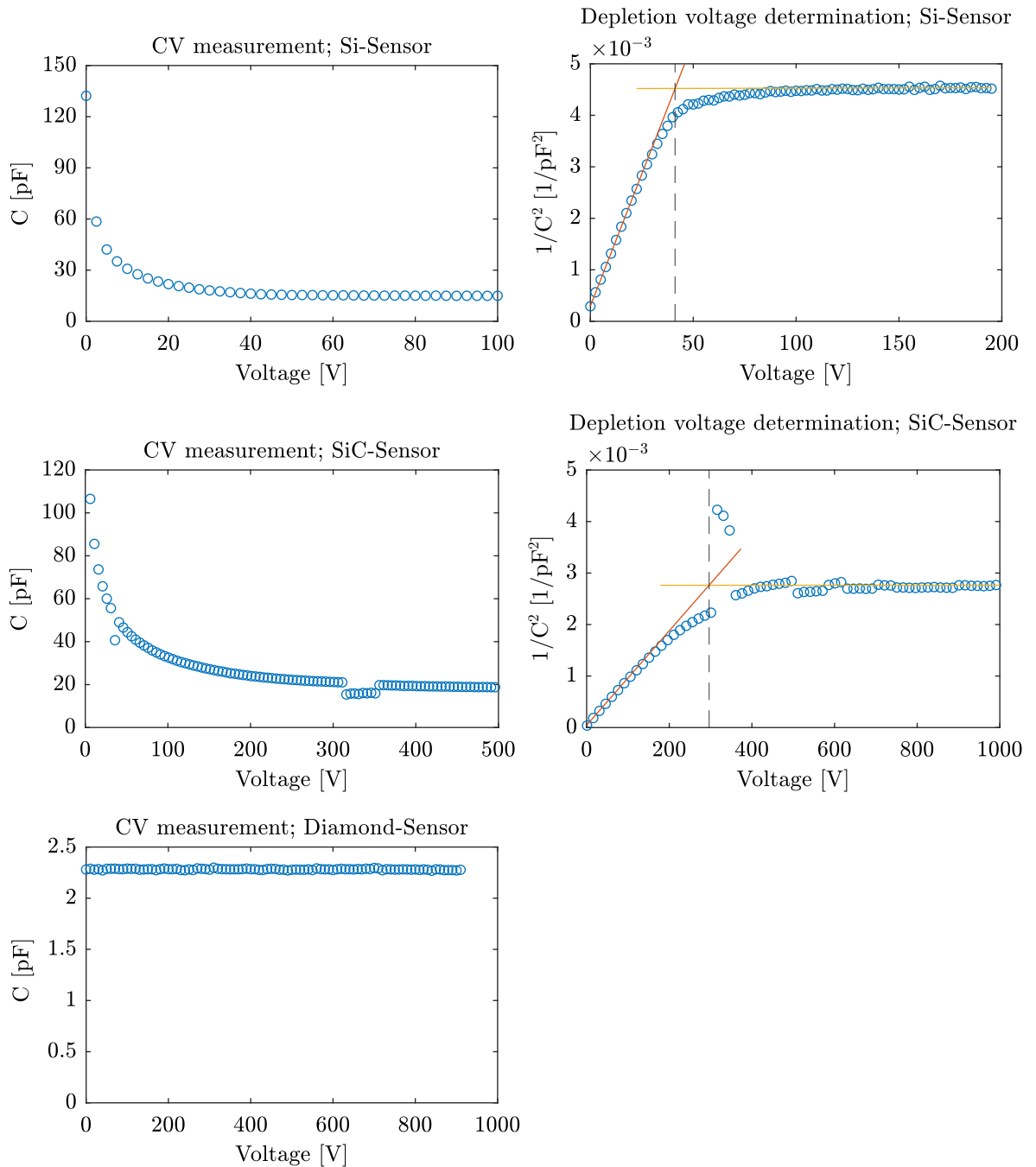


Figure 3.9: Shown are the capacitance voltage measurements (left) and the determination of the full depletion voltages (right). The capacitance was measured with the LCR meter of Figure 3.7. The dashed lines tag the full depletion voltages. Above: Silicon sensor; Middle: Silicon carbide sensor; Below: Diamond sensor. The silicon carbide capacitance measurement shows an unexplained discontinuity, which was also observed in multiple repetitions of the measurement.

3.6 Sensor simulations

To get an impression of the signal shapes produced by the different detectors when interacting with a MIP particle, the sensors were simulated in a program called Weightfield2 [48], which is based on ROOT and allows fast simulations by entering parameters into a QT-based graphical user interface.

It should be noted that a part of this project was dedicated to the fixing and improving of the program. The changes done here were then handed over to the development team and officially implemented during several releases.

3.6.1 Weightfield2

Weightfield2 can calculate the electric potential insight silicon (Figure 3.10), silicon carbide, LGAD, and diamond detectors after applying a bias voltage, which is done by discretizing and solving the Poisson equation:

$$\Delta\phi = -\frac{\rho}{\epsilon}, \quad (3.8)$$

where ρ is the charge density and ϵ the dielectric constant.

The associated electric field strength $\vec{E} = -\vec{\nabla}\phi$ is then used to simulate the charge collection process and the sensor output current resulting from an interaction with an ionizing particle. The output current can be further processed by a simulated electric readout circuit, such as a transimpedance amplifier and a charge-sensitive amplifier, resulting in an output voltage signal.

In order to start the simulation, several sensor, MIP particle and readout circuit properties must be specified. For this project the important parameters are the following:

- Sensor:
 - Material type: Si, SiC, Diamond
 - Doping type
 - Pitch and number of stripes (=1 single planar sensors)
 - Thickness and area
 - Gain properties (for LGAD)
 - Bias and full depletion voltage
 - Capacitance
- Readout electronics:
 - Gain, input impedance
 - Bandwidth

- Particle:
 - Selecting between MIP particles with fixed energy deposition per path length and a Landau distributed energy deposition
 - Energy deposition per path length
 - Number of simulated particle hits

The sensor parameters have been adjusted to match the properties of the silicon, diamond and silicon carbide detectors described in the previous sections.

The electrical parameters of the UCSC readout board, the one which was used in this project (see Section 4.1), are already defined internally in the program. The UCSC board must only be selected from a list of preconfigured readout circuits. Only the board gain was changed from the original value $4.7\text{ k}\Omega$, which is ten times higher than the value given by the developers [49], to $0.47\text{ k}\Omega$.

The particle settings were chosen to simulate for every sensor type 2000 MIP particle hits with a Landau distributed energy deposition. From those 2000 hits the average detector currents and readout output voltages are shown in the next section.

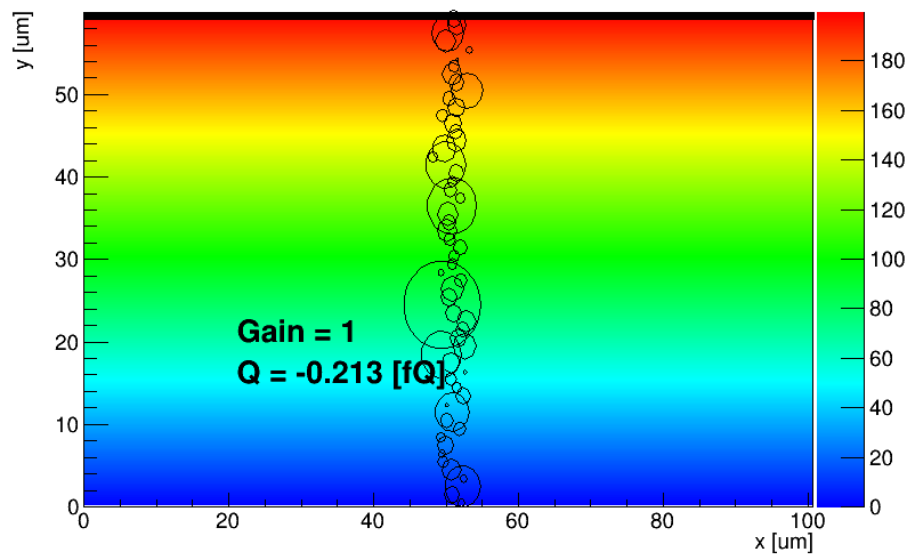


Figure 3.10: Shown is the simulated electric potential and the interaction with a MIP proton insight a silicon detector when operated at a bias voltage of 200 V. The black bubbles symbolize the amount of created charge carriers after an ionization event. It can be seen that the produced charge carrier amount is fluctuating and not constant, which results from a Landau distributed energy deposition (see Section 2.1.4).

3.6.2 Results

The result with bias voltages of 400 V (Figure 3.11) show that the mean silicon carbide output voltage signal is faster than the silicon and diamond detector signals. This can be seen through a comparison of the time periods in which the mean signals are above 10% of their maximum values (Silicon: 3.4 ns; Silicon carbide: 1.6 ns; Diamond: 5 ns). The output voltage graph also shown that the average SiC signal amplitude is only about half the size of silicon and about one-third of the diamond amplitude.

The total detector currents are a superposition of the currents produced by the moving electrons and holes (see Section 2.3.2). After some time, the electrons, which have higher mobility in silicon and silicon carbide than the holes, reach the end of the detector, and the contribution of the electrons to the total current disappears. From this point on, the total current equals the current produced by the holes. This can be seen as a kink in the current curves. Silicon carbide shows, for the simulations with a bias of 400 V, the highest current decreasing steepness, with is most probably due to the small detector thickness and a high electron mobility in SiC. As shown in equation 2.18 and 2.20, the steepness depends on the charge carrier mobilities, the electric field insight the detector, and the detector thickness.

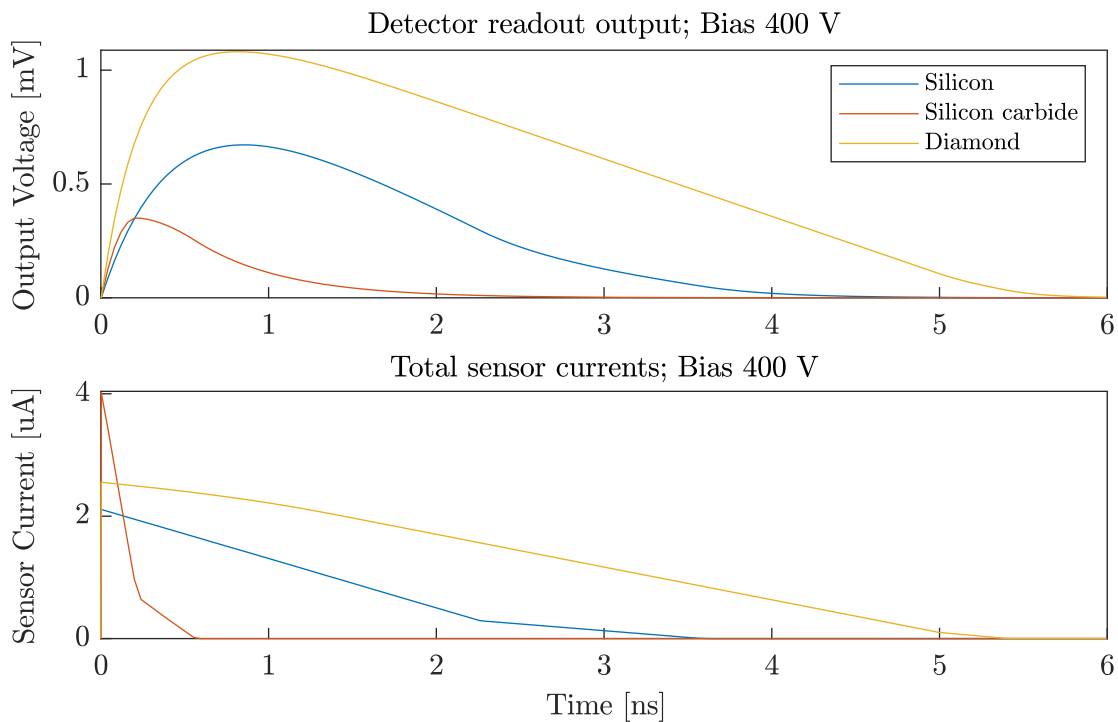


Figure 3.11: Shown are the Weightfield2 simulation results with bias voltages of 400 V of the diamond, silicon and silicon carbide sensors. The graphic above features the mean output voltages of the detector readout circuit and the one below the mean detector currents.

4 Readout electronics

The general purpose of a readout circuit is to take the output signals from one or more channels of a sensor and convert them to a format, which can be processed by the following electronics. Often this includes the signal preamplification, shaping and impedance adaptation.

The readout system used in this project is the UCSC (University of California Santa Cruz) board (Figure 4.1). The board converts charge accumulations of a single-channel detector at the input into a voltage signal at the output, which is achieved through a transimpedance amplifier. Essential parameters of the amplifier are the transimpedance and the input impedance. The input impedance directly influences the signal duration because the sensor capacitance has to discharge itself over it (see Section 2.3.3). The resulting current is then converted into an output voltage with the transimpedance as proportionality factor $U_a = I_i Z_T$. Hence, the transimpedance corresponds to the level of amplification. Due to their importance, both are determined by simulations in Section 4.2.1 and for both are approximated equations given in Section 4.1.1.

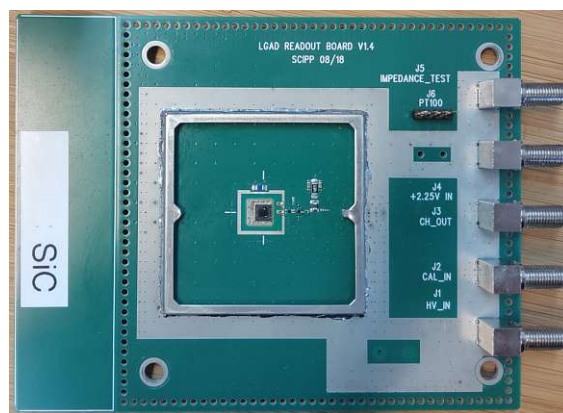


Figure 4.1: The UCSC board equipped with the silicon carbide sensor

4.1 The UCSC board

The UCSC board was developed by the University of California Santa Cruz (UCSC) and is often utilized in combination with LGAD sensors, therefore it is also referred to as LGAD board. The central part of the board is a single-stage inverting transimpedance amplifier with a schematic shown in Figure 4.3. The amplifier uses the silicon-germanium transistor "BFR840L3RHESD" from Infineon, which has a transition frequency of 75 GHz. If used with a feedback resistor R_{14} of $470\ \Omega$ and terminated with $50\ \Omega$, the transimpedance of the amplifier is $470\ \Omega$ within a bandwidth of 1.6 GHz (according to the documentation [49]). The transimpedance and therefore the amplification can be adjusted by changing R_{14} . Above the transimpedance amplifier, an additional circuit (containing C35, C36 and L5) is responsible for smoothing the external supply voltage of 2.25 V, which is needed by the amplifier.

The sensor is placed at the metallic contact in the middle of the board, which lies on the potential of the HV input. The detector top side is connected by wire bonds to the transimpedance amplifier circuit and over a $1\ \text{M}\Omega$ resistor to the ground, biasing so the sensor.

The introduction of external noise is reduced by attaching a shield on both sides of the board, covering the electronics beneath it. In this shield, a 3 mm diameter hole is drilled, which allows the particles to pass through unobstructed.

Knowing the structure of the PCB board is essential to conduct the simulations of Section 4.2.1. The separate layers are shown in Figure 4.2. Together they result in a total thickness of 1.6 mm.

15 μm laccquer
35 μm chopper
376 μm prepreg
18 μm chopper
710 μm FR4
18 μm chopper
376 μm prepreg
35 μm chopper
15 μm laccquer

Figure 4.2: The different layers of the UCSC PCB board

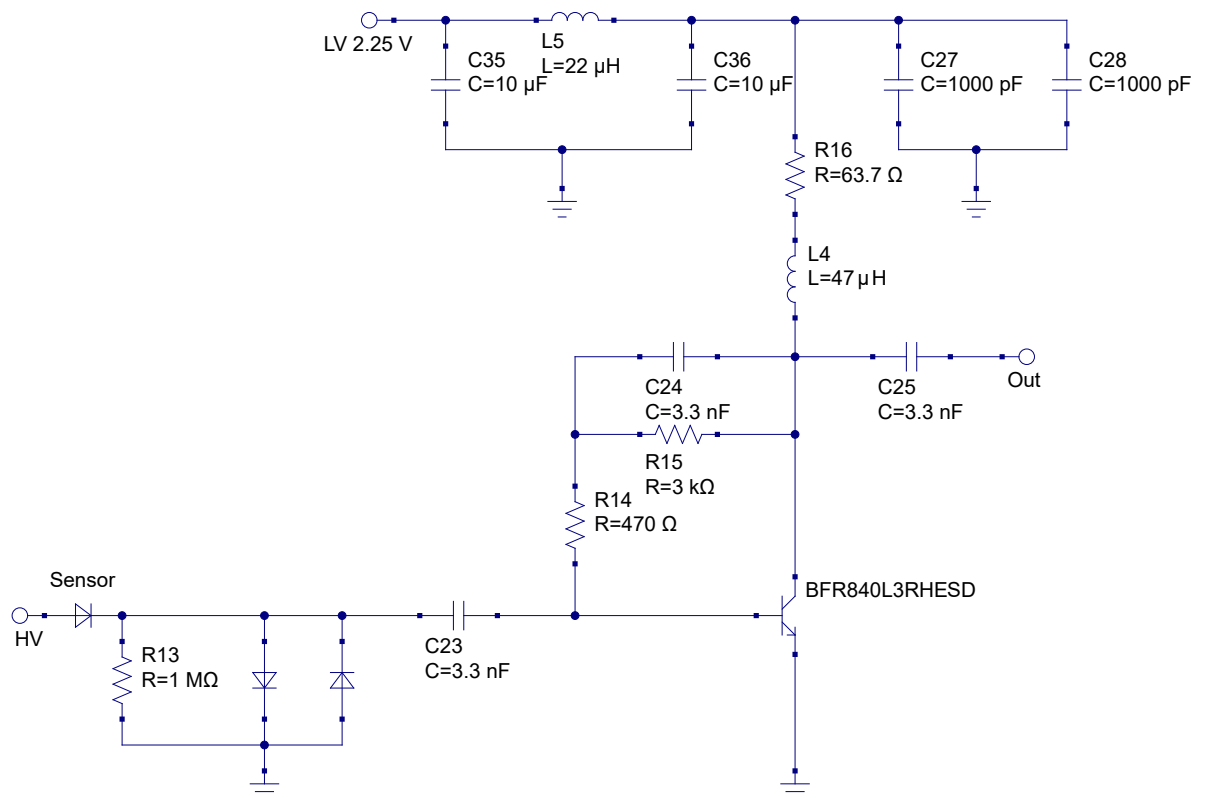


Figure 4.3: Shown is the schematic of the UCSC board transimpedance amplifier and the low supply voltage smoothing circuit.

4.1.1 Theoretical analysis

In order to calculate the amplification, several simplifications are done:

- The impedances of all capacitors are at the operation frequencies equal to zero
- The coil L_4 "GLF201208T470M" is operated at a frequency where the parallel parasitic capacitance is predominant. A value around $C_p \approx 2.3$ pF is assumed from the measurements listed in the corresponding datasheet. Therefore, it is assumed that the coil is shorted for the operation frequencies (> 100 MHz).
- The other components are considered as ideal
- No line reflections

With that, a equation for the input impedance \underline{Z}_I and the transimpedance \underline{Z}_T can be found through a small signal analysis:

$$\underline{Z}_I = \frac{U_i}{I_i} \approx \frac{r_{BE}[R_{14} + \underline{Z}_L || R_{16}]}{r_{BE} + R_{14} + (1 + \beta)[\underline{Z}_L || R_{16}]} \quad (4.1)$$

$$\underline{Z}_T = \frac{U_a}{I_i} \approx \frac{\underline{Z}_L R_{16}[r_{BE} - \beta R_{14}]}{R_{16}[r_{BE} + R_{14}] + \underline{Z}_L[r_{BE} + R_{14} + R_{16}(1 + \beta)]} \quad (4.2)$$

In the equations, β denotes the AC current gain and r_{BE} the base emitter resistor of the transistor, all other components are named as in Figure 4.3. In the calculation it was assumed that $r_{CE} \gg \underline{Z}_L, R_{16}$. If the current gain is high enough so that the terms without β in the denominator can be neglected, equation 4.2 can be further simplified:

$$\underline{Z}_T \approx -R_{14} \quad (4.3)$$

So it can be seen, that for not too high R_{14} values, the transimpedance is proportional to the feedback resistor. The feedback resistors has by default a value of 470Ω , but as shown, the amplification can be raised by increasing its value.

4.2 Circuit simulations

Simulations provide a way to determine the properties of an electrical circuit. In addition, the effects of changes and possible optimizations can be investigated. In this project, the challenge lies in the readout board's high operating frequency (> 100 MHz); lines and components cannot be considered as ideal and high frequency effects must be included. Some commercial programs that offer simulations in such high-frequency ranges are RF.Spice, Advanced Design System (ADS), and Microwave Office. Two examples of free-to-use programs are Qucs and QucsStudio. Both of those programs share the same roots, but unlike Qucs, QucsStudio is not developed by an open community, and its source code is not public.

The free-of-charge use and the open-source code are the reason why Qucs was chosen for this project.

4.2.1 Qucs

Qucs (Quite Universal Circuit Simulator) [50] is an open-source, integrated circuit simulation program with a graphical user interface. Qucs is similar to SPICE, but with some high-frequency extensions. So it is possible to perform simulations in the high-frequency range (> 100 MHz) by simply using the corresponding high-frequency components. Thus are, for example, microstrips, non-ideal capacitors with Q-factors, non-ideal coils, and bonding wires. With circuits containing those components, it is possible to conduct several simulations like AC, DC, S-parameter, Harmonic Balance, and noise analysis. Additionally, equations can be defined, which are solved in every simulation step. Another possibility is to define sweep parameters. Sweep parameters allow performing simulations multiple times with different parameter values. In this project, the R_{14} value was such a sweep parameter. Its value was set to $470\ \Omega$, $2.2\ \text{k}\Omega$ and $10\ \text{k}\Omega$.

Before conducting simulations, some of the ideal components of the board schematic had to be replaced with nonideal models. These are the connecting lines, the transistor, the coils, and the capacitors. Most of the contacts on the UCSC board are realized with microstrips. In Qucs, microstrips require a substrate specification. Such a substrate fills the space between the signal line and the ground plane and can be seen in Figure 4.2 tagged with the prepreg name. The connection lines going to the input and outputs are realized with striplines. Because they are not available yet in Qucs, they are modeled with general transmission lines with the corresponding stripline wave impedance. The transistor itself was simulated with a model from Infineon, and the coils and capacitors were replaced with equivalent circuits, imitating some of the nonideal effects. The output of the board is connected to a $50\ \Omega$ resistor, which equals the input impedance of the oscilloscope or the Cividec amplifier connected in the measurements of Section 5.

To conduct DC and AC simulations with the resulting simulation circuit (Figure 4.4) an AC supply, from which the frequency is changed in configurable steps in the AC simulation, was connected to the input of the transimpedance amplifier and two equations were defined, which calculate the input impedance and transimpedance for every single step.

The output of the simulations is the input and transimpedance value for different operating frequencies and different R_{14} values.

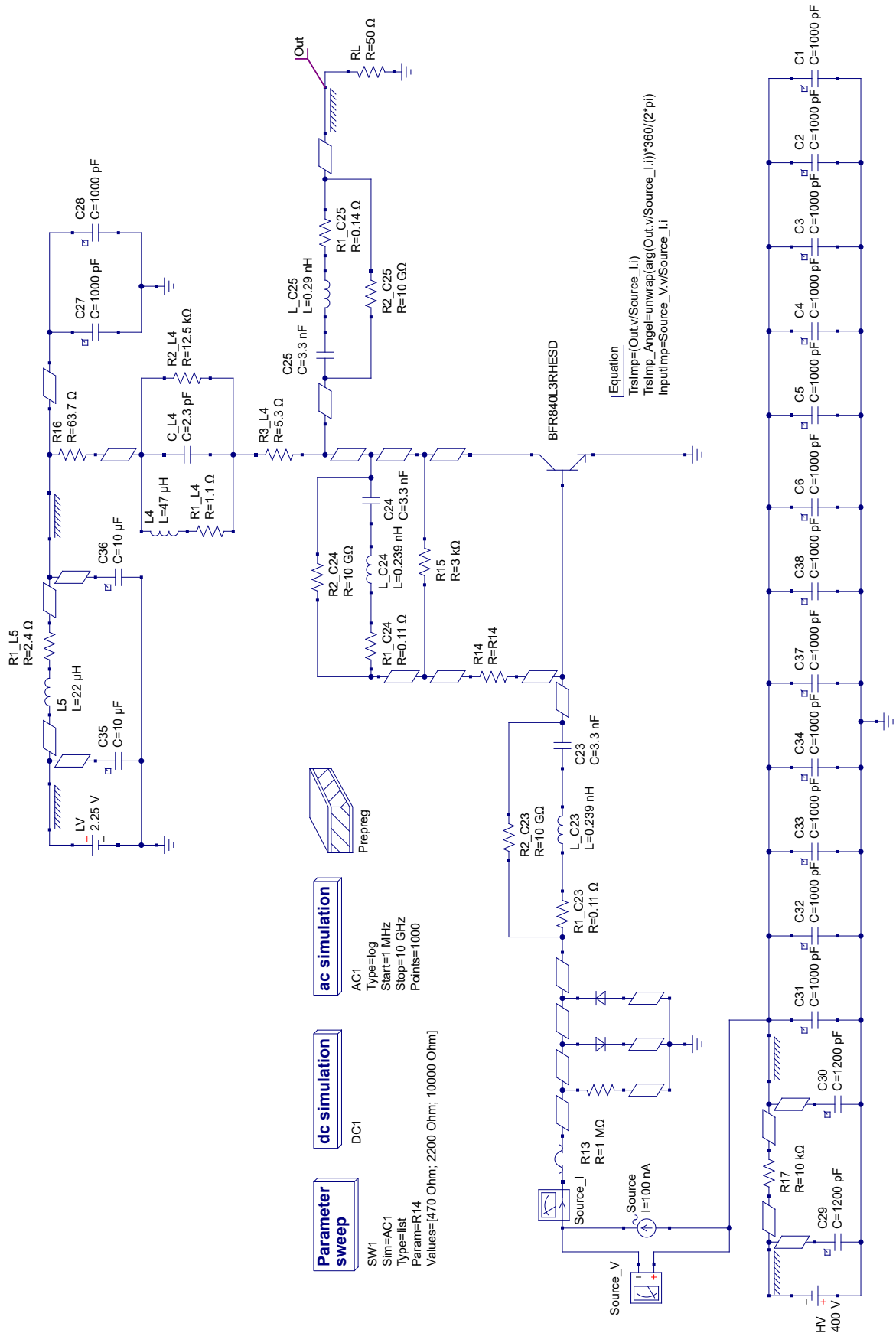


Figure 4.4: Shown is the Qucs UCSC board simulation circuit. Non-ideal properties of the transimpedance capacitors and coils were simulated with equivalent circuits. The parallelogram-shaped components denote the microstrips. Stripline connections were modeled with general transmission lines with the corresponding stripline wave impedances.

4.2.2 Results

It can be seen, as expected from the calculation in Section 4.1.1, that the transimpedance is increased for higher R_{14} values (Figure 4.5). At the same time, the input impedance also rises and the bandwidth shrinks, which reduces the dynamic of the UCSC electronics. Therefore, a compromise between signal height and duration must be found.

The amplification bandwidth, the transimpedance, input impedance and the ratio of those two (ratio = Z_T/Z_I) insight the bandwidth for different R14 resistors are given:

R_{14} [Ω]	bandwidth [MHz]	transimpedance [Ω]	input impedance [Ω]	ratio [1]
470	3300	418	27	15.5
2200	730	1685	104	16.2
10000	265	4920	350	14.1

Table 4.1: Shows the results of the readout board simulation done in Qucs.

The highest ratio is achieved with a R_{14} of 2.2 k Ω , which can be seen in consequence as good compromise between duration and amplification and was therefore chosen to be used in the measurements of Section 5.

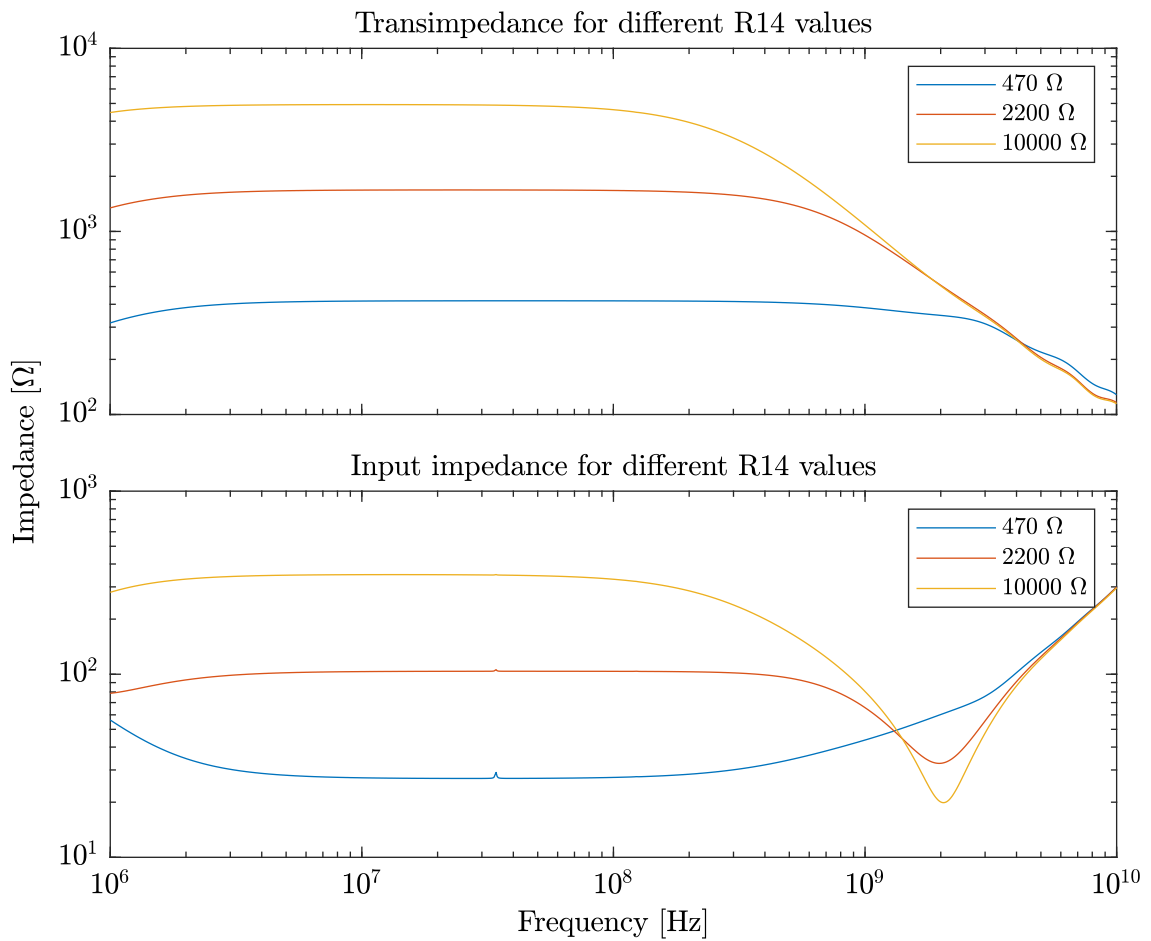


Figure 4.5: Shown are the Qucs simulation results of the UCSC board. The upper graph features the frequency dependence of the transimpedance, and the lower graph the frequency dependence of the input impedance for different R_{14} values.

5 Measurements

The central task of the measurements was to capture and examine the signal properties from the different detectors in different setups. In order to do so, the sensors were operated in the laboratory with an α and a β source as well as at MedAustron in the beamline. The corresponding measurement setups and their results are shown in this chapter. But before discussing the measurements in detail, general information concerning all measurements is given.

The sensor signals were captured with the Tektronix DSA 70804 oscilloscope (Bandwidth: 8 GHz). The oscilloscope was controlled over a PC with a python script, which was developed especially for this project. The communication between the PC and the oscilloscope is running over an ethernet connection. In a capturing process the signals are first buffered in the oscilloscope. After capturing a certain amount of events, they are then transferred together with trigger information (type, level, timestamps, source-channel) and the sampling rate to the PC.

Additionally to the oscilloscope, the amplifier "C2-HV" (Bandwidth: 2 GHz, Gain: 40 dB) from Cividec was used, which allows a linear 40 dB amplification of the voltage signal coming from the UCSC board. The linearity is restricted to a Cividec output voltage between approx. +/- 1 V. The signals produced by the α source exceed this limit; this is why the additional amplifier was used in every measurement except those including the α source.

As described in Section 3.2, the diamond sensor must be "pumped" before conducting measurements. Therefore, the sensor was exposed, before each measurement, for four hours to the radiation of a Sr-90 source with an activity of 370 MBq (measured at the time of acquisition 1982).

The HV input voltage polarity of the UCSC board (see Section 4.1) was always chosen in a way that the sensor is operated in reverse direction. In the case of the diamond sensor negative voltages were used with respect to the ground voltage of the UCSC board.

To increase the comparability between the different sensors, all output voltages are shown with positive polarity, regardless of the measured polarity. That means, that the silicon carbide and diamond signals were digitally inverted in a post process.

5.1 Measurements with radioactive sources

The measurements in the laboratory with the radioactive sources can be divided into two setups: First, the spectrum of the α source Am-241 was measured with the diamond,

silicon and silicon carbide sensor at different bias voltages. Then, all these sensors were operated in the so-called beta telescope, which permits capturing only signals produced by electrons with MIP behavior from the Sr-90 spectrum (see Section 2.4.2).

5.1.1 Americium-241

The Am-241 α source enables the measurement of higher signal amplitudes than those produced by traversing MIP particles. In general, the discrete energy spectrums of α sources can also be used for a characterization of a detector setup and thus to get a direct mapping of deposited energy in the sensor to the resulting output voltages (see Section 2.4.1).

Setup

The setup used for these measurements can be seen in Figure 5.1. The corresponding DUT (device under test) sensor is operated with the UCSC board and supplied by bias voltages from 100 V - 400 V. The Americium-241 source is placed above the detector. When a particle hits the sensor, the produced signal is fed directly into the Tektronix oscilloscope without a second amplification. If the signal is above the configured trigger level, its waveform is captured. After capturing a certain amount of hits, the signal forms are transferred and saved to a PC. There the maximum value of every signal is determined and put into a histogram. This process was conducted with the silicon, silicon carbide and diamond sensor. The trigger levels were chosen to capture only particle signals and had the follow values:

Bias voltage [V]	Silicon [mV]	Silicon carbide [mV]	Diamond [mV]
100	2.2	4.4	3
200	2.2	4.4	2
400	2.2	4.4	2

Table 5.1: Shown are the oscilloscope trigger levels used in the Am-241 setup. The trigger levels were chosen to capture as many particle signals as possible while pure noise signals are ignored.

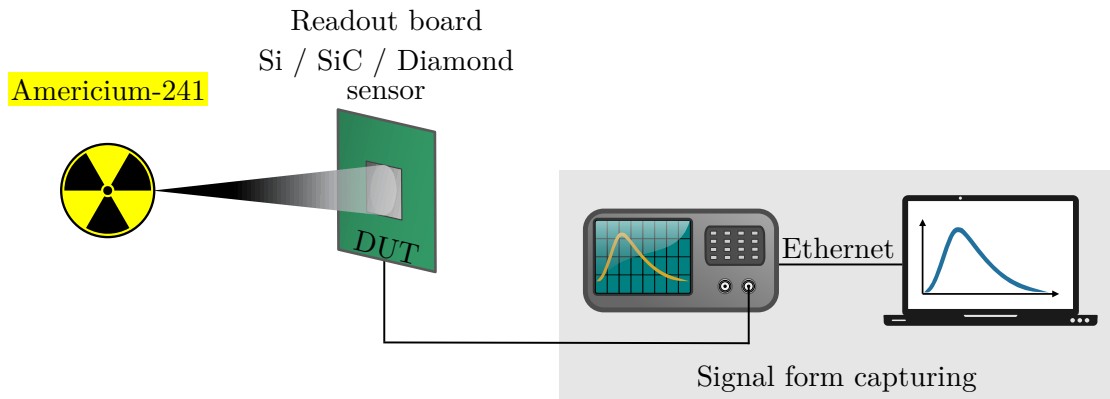


Figure 5.1: Measurement setup to capture signals produced by particles from the Am-241 source

Results

The sensor signal amplitudes are proportional to the alpha particle energies. As described in Section 2.4.1, the alpha energy spectrum becomes continuously distributed around the discrete decay energy values due to scattering processes in the Am-241 material and in the air, which can also be observed in the amplitude distributions (Figure 5.2). Therefore, only an approximate characterization of the detector systems can be done.

Higher bias voltages cause a shift to higher signal voltages in all sensors. In the diamond sensor and the silicon sensor (already fully depleted above 44 V), this is only a consequence of faster charge extraction. In the silicon carbide sensor, the depletion zone increases up to 296 V, which leads to an additional amplification.

It is likely that the two peaks in the silicon carbide spectrum are a consequence of the two highest decay modes of the Am-241 decay (Figure 2.12). A considerable part of signals produced by alpha particles from the primary decay mode lies below the trigger level. The peak on the right belongs then to particles from the rare highest decay mode. The right shift after increasing the bias voltage leads to the fact that more and more of the main decay mode signals are triggered, and so the relative amount of captured high mode signals declines.

The reason why the signal amplitudes in the case of the diamond sensor seem to be higher than those of silicon carbide is not fully understood. Comparing the energies needed to generate a charge pair, one would expect the opposite (Diamond: 12.86 eV; Silicon carbide: 7.28 eV) (see Chapter 3). The fact that diamond has the largest active thickness (500 μm ; see Section 3.2) cannot be the reason, because the alpha particles already deposit their whole energy in thin sensor layers ($\approx 30 \mu\text{m}$ in silicon; see Section 2.4.1). Another explanation could be that in the diamond spectrum, only the peak from the rare higher energy decay mode is visible. That would mean that the amplitudes of the main decay mode are not high enough to even reach the trigger level.

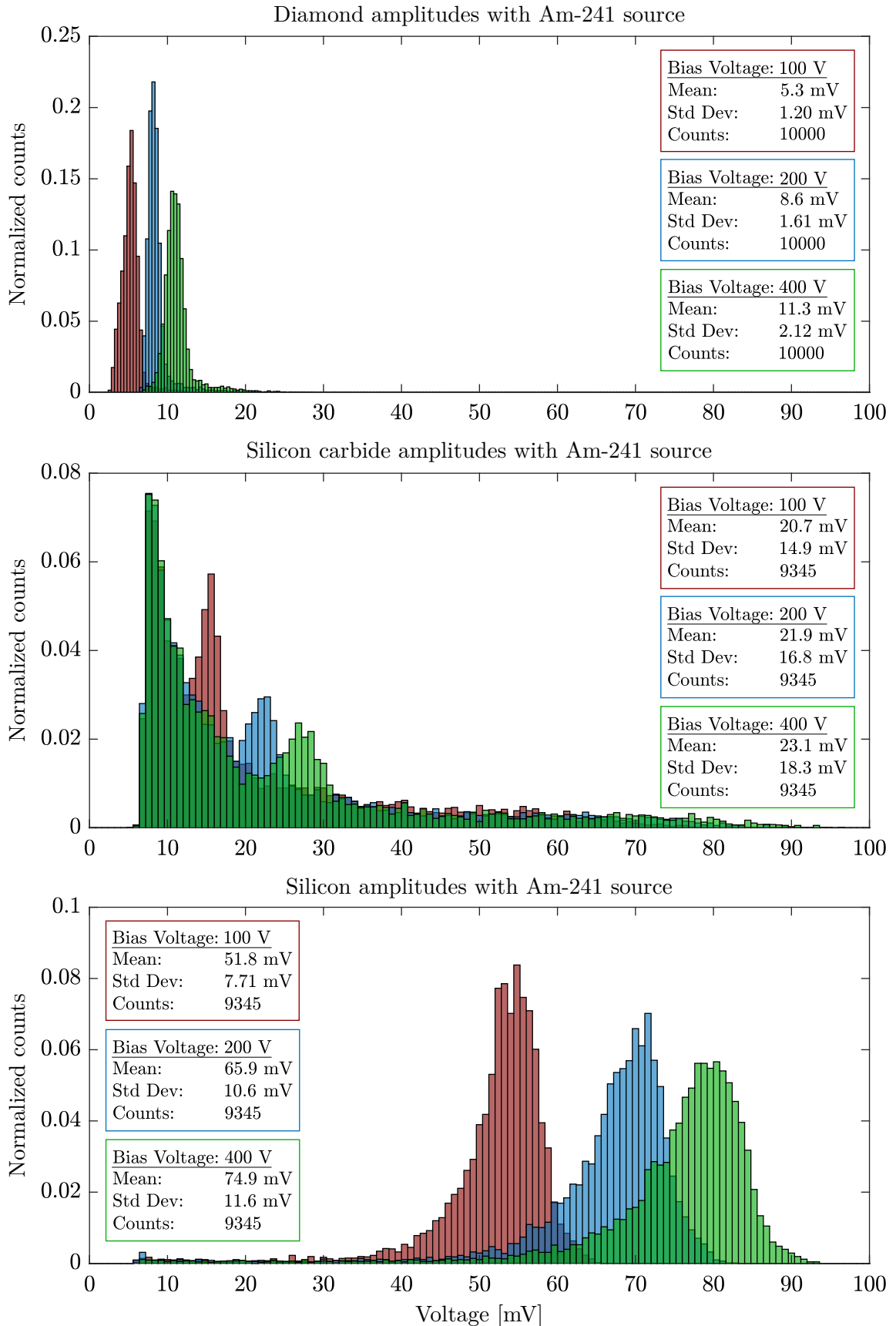


Figure 5.2: The histograms show the distributions of the signal max. values for different bias voltages (100 V, 200 V, 400 V) and sensors (upper: Diamond, middle: SiC, below: Si). The count values give the number of waveforms, which were captured. In addition, the mean and standard deviation are shown.

5.1.2 Beta telescope

As described in Section 2.4.2, Sr-90 and its decay product Y-90 emit electrons with a continuous spectrum of energies. Only the electrons of the upper part of the spectrum have enough energy to show MIP behavior. The setup of Figure 5.1 must therefore be adjusted to capture only signals from those electrons. The result is the so-called beta telescope.

Setup

In the beta telescope setup, the DUT sensor is placed above an LGAD sensor (Figure 5.3 and Figure 5.4). From the emission spectrum of the Strontium-90 source, only MIP particles can travel through the DUT sensor, both PCB boards and produce a signal on the LGAD detector (see Section 2.4.2) on the backside. This signal is then used to trigger the Tektronix oscilloscope, which captures the signals amplified by two Cividex amplifiers of both sensors. In this way, only signals of MIP particles are captured, while other signals are ignored. After capturing a certain number of waveforms, they are transferred to a computer, where every signal's amplitude is determined and plotted into a histogram. This process is repeated for different bias voltages 100 V - 400 V for the silicon, silicon carbide, and diamond sensor as DUT.

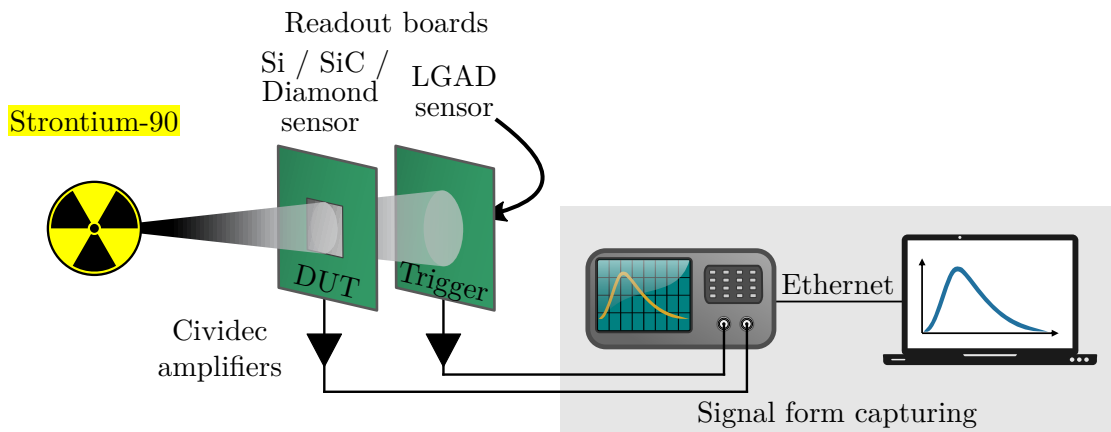


Figure 5.3: An illustration of the used beta telescope setup

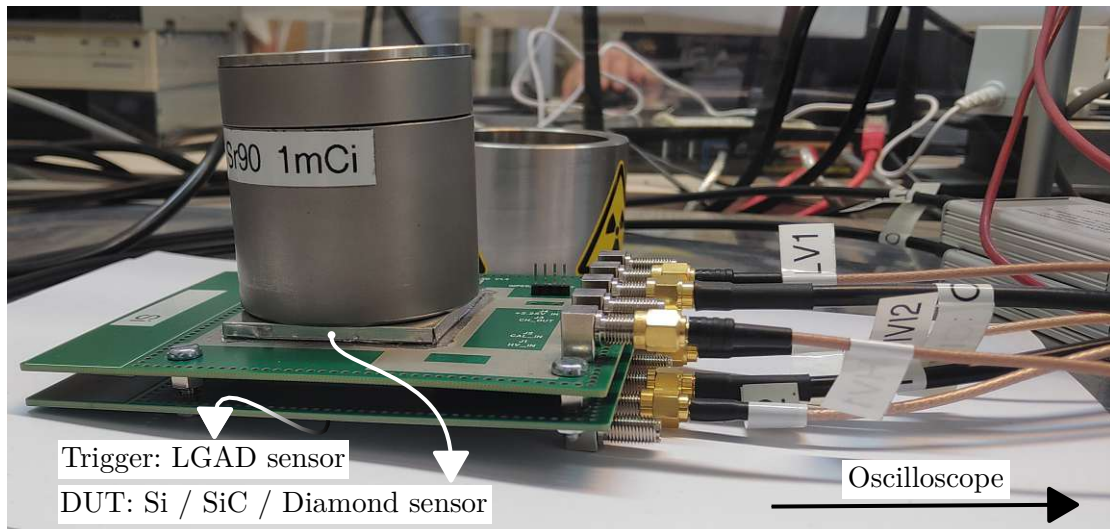


Figure 5.4: The beta telescope build up in the laboratory

Results

The energy deposition in thin material layers of particles with uniform energy follows a Landau function (Section 2.1.4). The superposition of a Landau with Gaussian noise results in a Langau distribution. Such Langau can be seen in the silicon result of Figure 5.5. Therefore, the part of the histogram belonging to the Langau, tags signals from particle hits. The Langau is separated from pure noise records on the left. In those noise records, the Landau part is missing, and only the Gaussian distributed noise remains. The Gaussian parameters remain nearly unchanged for all three bias voltages, while the Langau distribution is shifted to higher amplitude values (indicated by dashed lines). This is consistent with the fact that the signal amplitudes are increased for higher bias voltages due to a faster charge extraction (Section 2.3.2).

The signals produced by MIP particles in the silicon carbide sensor and the resulting signal-to-noise ratios are insufficient to distinguish pure noise from particle hits in the distribution (Figure 5.6). This is in contrast to the measurements conducted with the silicon sensor. Except for a slightly growing standard deviation, there cannot be seen any difference between the distribution of the randomly triggered amplitudes and the histogram triggered by the LGAD sensor.

The diamond sensor shows, like the silicon sensor, a Langau distribution (Figure 5.7). But contrary to the silicon distribution, the spectrum doesn't indicate a clear separation between a Gaussian and Langau part. The measurement with the random trigger shows that the signal-to-noise ratio is high enough to see two different peaks in the spectrum if particle signals and pure noise signals would have been captured. Therefore it can be concluded that every particle triggering the capturing had also produced a signal in the diamond, and no pure noise signals were captured.

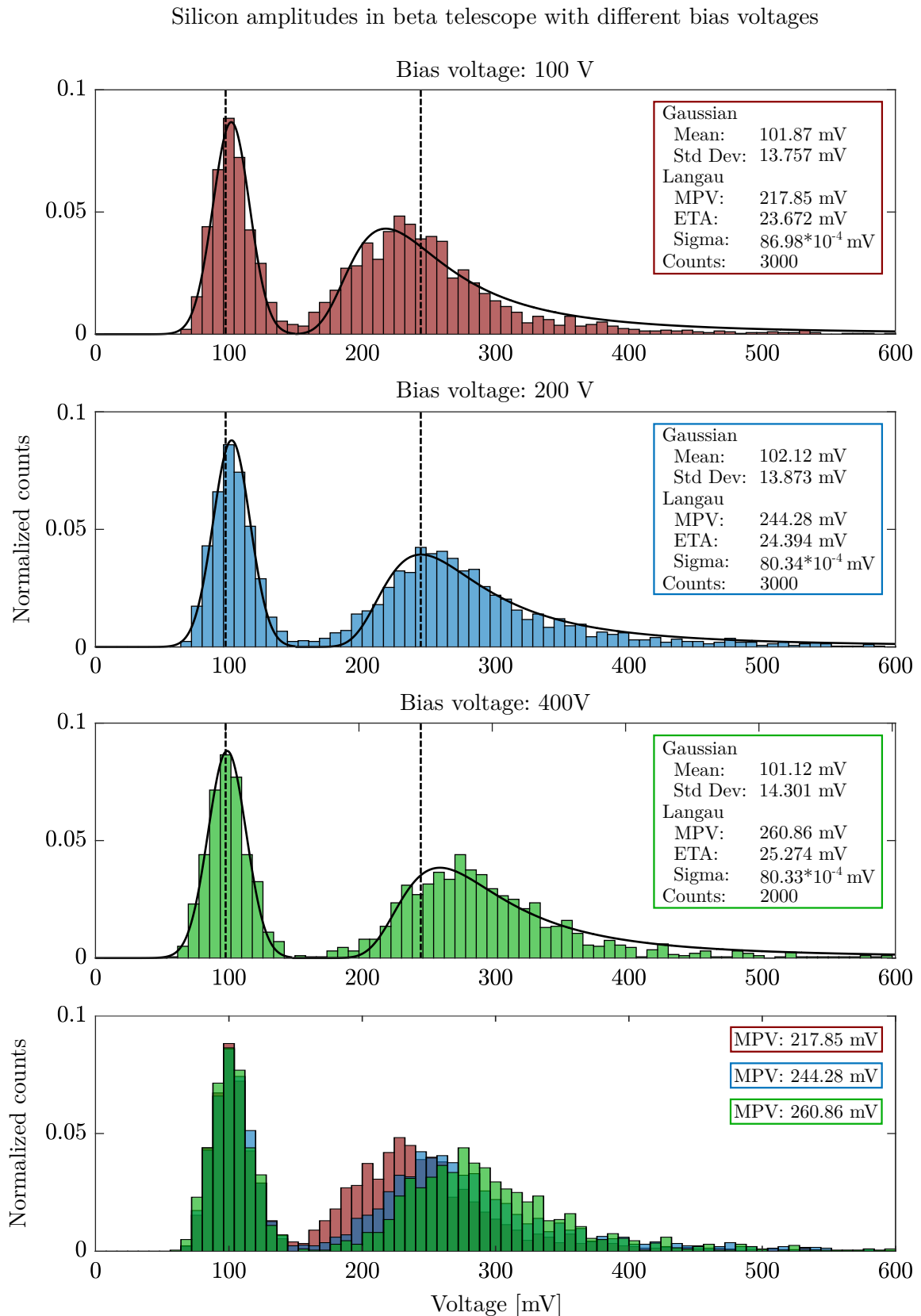


Figure 5.5: Shown is the signal amplitude distribution of the silicon sensor for different bias voltages produced by MIP particles. The histograms are split into two parts, separated by a gap containing signal amplitudes, which occur more rarely. Gaussians were fitted on the distributions on the left sides (<150 mV). For the right sides, the amplitudes with higher voltages (>150 mV), Langau fits were chosen. The fit parameters of the Gaussian and the Langau parts can be found in the corresponding diagrams.

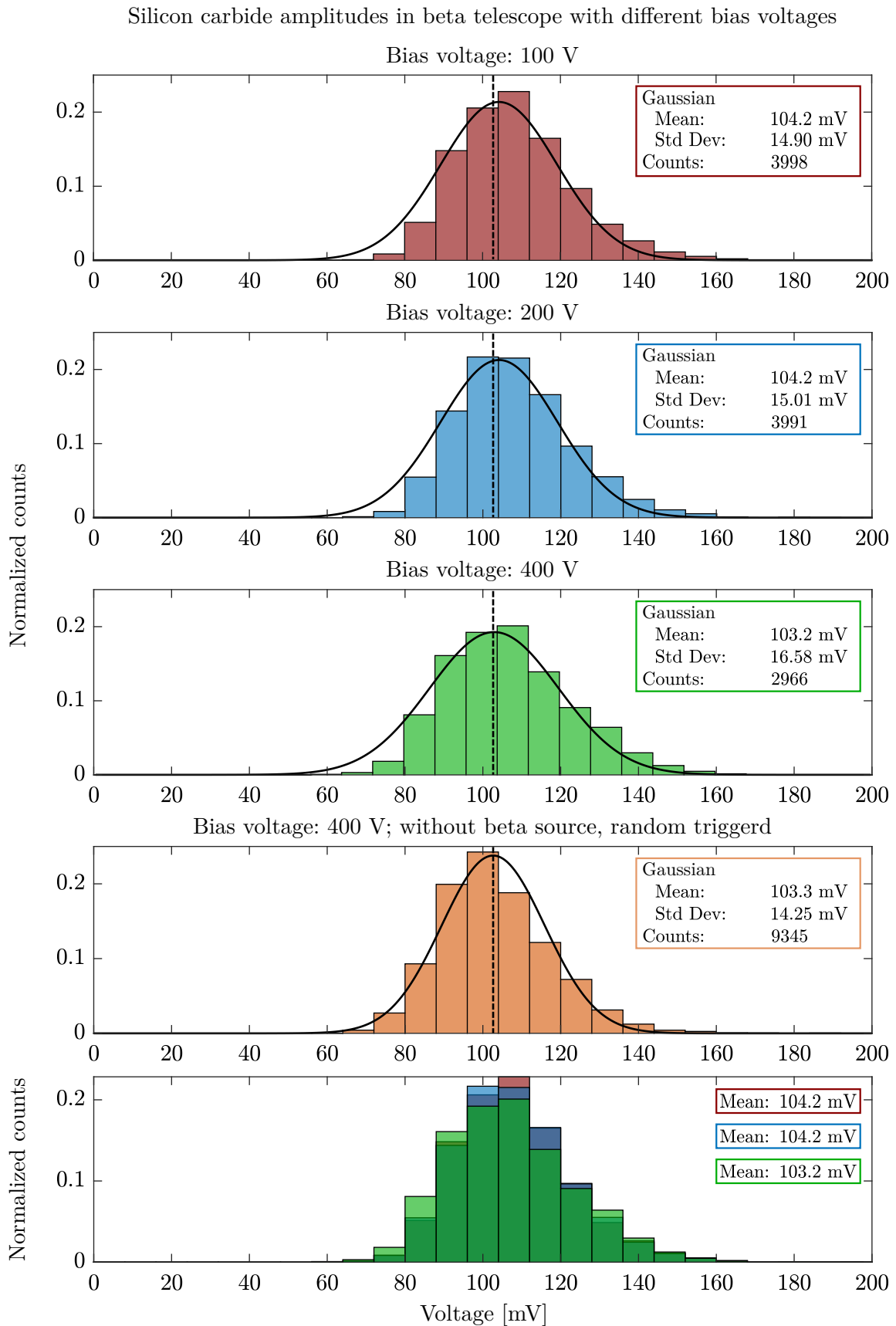


Figure 5.6: The Figure shows the amplitude distribution of silicon carbide and their Gaussian fit functions for different bias voltages. A random trigger signal capturing was also conducted to compare the pure noise distribution with the measured one. The oscilloscope is here not triggered by a particle. Instead, the voltage output of the detector system is captured randomly in the absence of particle signals (see the fourth diagram).

Diamond amplitudes in beta telescope with different bias voltages

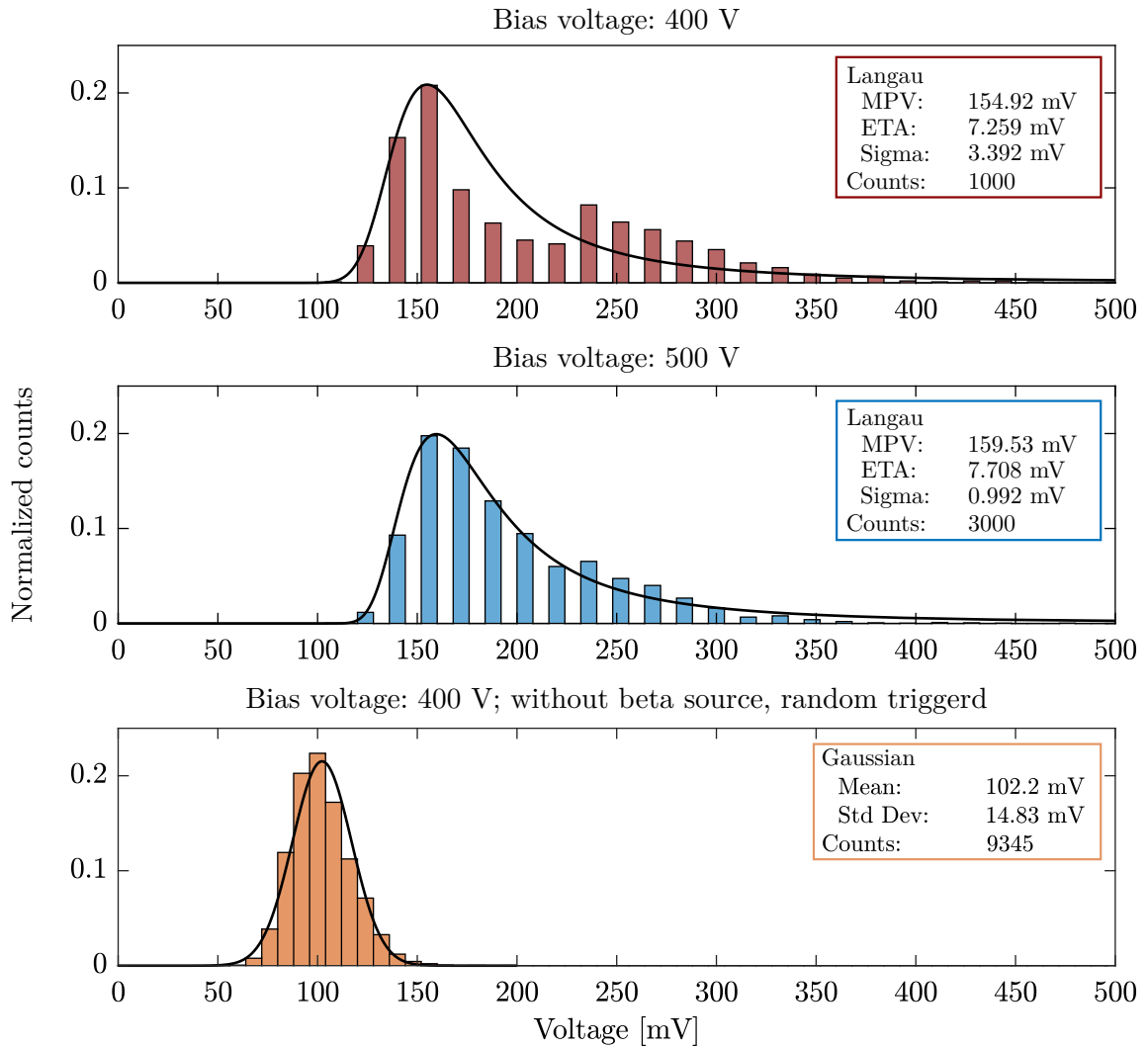


Figure 5.7: The amplitude distribution of diamond for bias voltages of 400 V and 500 V, on which Langau fits were applied. The Langau parameters are shown in the respective graph. In addition, the noise distribution, which was captured with a random trigger, for a bias voltage of 400 V is shown.

5.2 Measurements at MedAustron

The measurements presented in this section were conducted at the IR 1 (irradiation room) of the cancer treatment and research facility MedAustron, located in Wiener Neustadt (Austria). Compared to the radioactive sources, the beam there has the advantage that particle energies and intensities can be varied in a wide range, which enables the investigation of the sensor signals in multiple operating modes.

Besides the used IR 1, which is reserved for non-clinical research, MedAustron has three additional rooms (IR 2, IR 3, IR 4) exclusively for treatments and clinical research. Currently MedAustron offers proton and carbon particle beams. The particles are provided by two ion sources and accelerated first by an interdigital H-mode linear accelerator (LINAC) and then by a synchrotron. From there, they are extracted and transferred to one of the irradiation rooms. A device called degrader can be found between the LINAC, and the synchrotron. This device allows the adjustment of the number of particles going to the synchrotron and, therefore, the beam particle rate. Possible settings are 10%, 20%, 50% of the nominal intensity [3]. As stated in Section 2.2.2, nominal intensities for medical treatments around 0.1 GHz to 1 GHz are used. In the progression of various projects, such as the pCT project [17], the need has emerged to operate the beam at lower intensities. The result was the so-called low-flux settings (Figure 5.8). Here is the beam intensity reduced through different accelerator configuration adjustments. The low flux settings include three different intensities, which in turn can be operated with eight different particle energies [3].

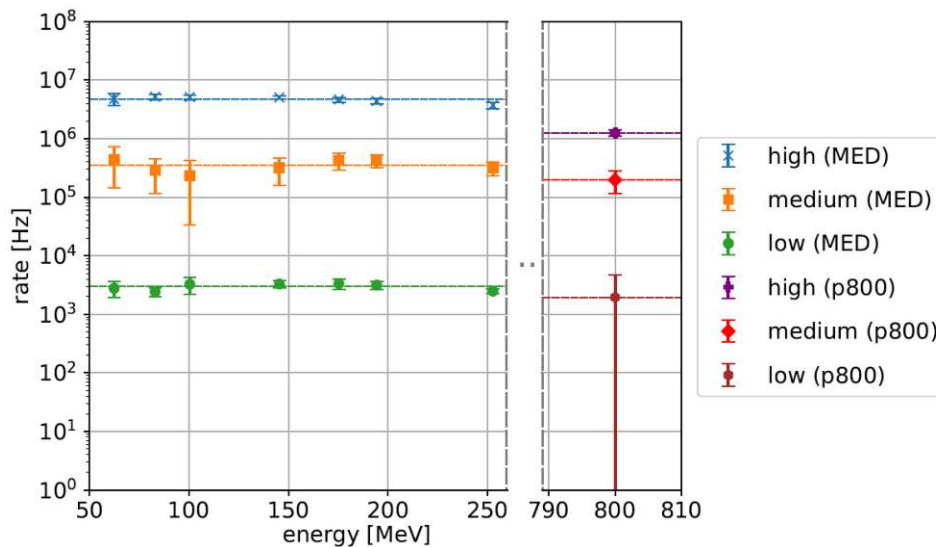


Figure 5.8: Given are the available low flux settings at MedAustron. (Kindly provided by [3])

5.2.1 Setup

At MedAustron, the silicon carbide (upstream) and silicon sensor (downstream) were operated in-line in a proton beam. The bias voltages of both sensors were kept constant at 400 V. The silicon waveforms measurement data shown in the result section were captured with the silicon carbide sensor as trigger and vice versa. The oscilloscope captured then a certain number of both waveforms. At the same time, the signals were first discriminated by two comparators (MAX40025) and then processed by an MPSoC (Multiprocessor system on a chip) module named "TE0820-03-2BE21FA". One of the main component of the module is the Xilinx Zynq UltraScale+ ZU2EG-1E. The "Xilinx Zynq UltraScale+ ZU2EG-1E" in turn consists of a PS (processing system) and a PLD (programmable logic device) unit. The PLD or LGAD unit counted the hits and recorded the total time-over-threshold (ToT), these functionalities were implemented during the bachelor thesis [51]. Both values were then handed over to the PS unit with a local timestamp (1.5 GHz clock count). The information was periodically transferred over UART to a PC, where the whole data was stored and the hit rates displayed. The data transfer and display was managed by a python script, which was developed in this project (Figure 5.10). The IR1 beam room can not be entered while the beam is active, which means that the whole setup had to be controllable from remote. The PCs communicating with the oscilloscope and FPGA were operated in the beam room and monitored from the control room by VNC over the local network. Also, the bias voltages and discriminator thresholds were set from there.

Before reaching the silicon carbide sensor, the proton beam characteristics were altered by traveling through two ripple filters. Those filters are made of PMMA (poly methyl methacrylate) and have an average thickness of 1.28 mm. The properties of the beam hitting the silicon sensor were further changed by the silicon carbide and the UCSC PCB board material. The effects of those interactions were determined through simulations of the whole setup in a program called Gate [52].

Gate is an open-source program based on the Geant4¹ toolkit and was created by the OpenGate collaboration. It can conduct simulations for medical physics applications and was developed especially for the subjects of emission tomography, computed tomography (CT), optical imaging and radiotherapy experiments. In this project, it was used in a more physical approach. Namely, after defining the geometrical properties of an experiment and the characteristics of a particle source in so called .mac (macro) files, Gate simulated the path of emitted particles through the setup and provided, as output, among other things, information about the particle trajectories and their interaction with the matter.

The used Gate application was derived from the proton simulations of the bachelor thesis [28]. For this project the geometrical setup was adjusted to reflect the configuration of Figure 5.9 plus the above described ripple filters. Important results of the simulation were the modified particle energies and their spatial distributions. These corrections were used in the calculation of the results Figure 5.13 - Figure 5.15.

¹"a toolkit for the simulation of the passage of particles through matter" [53] by using Monte Carlo methods

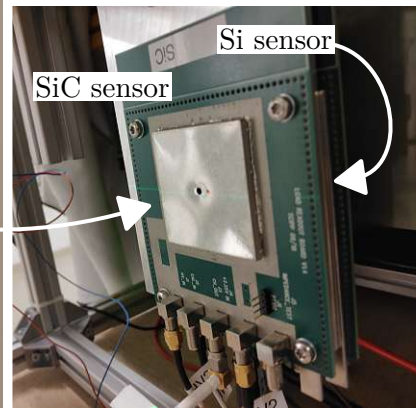
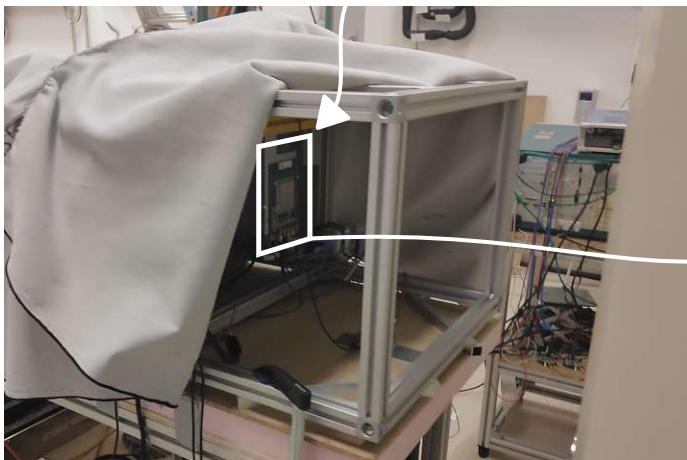
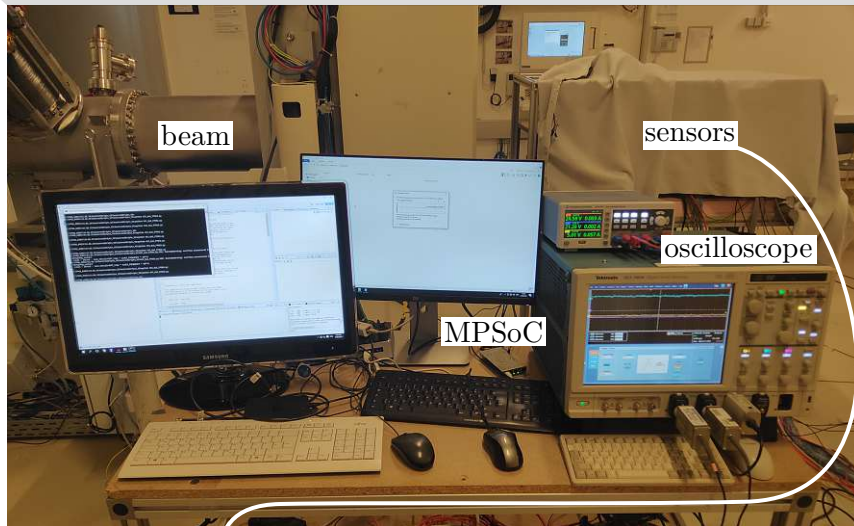
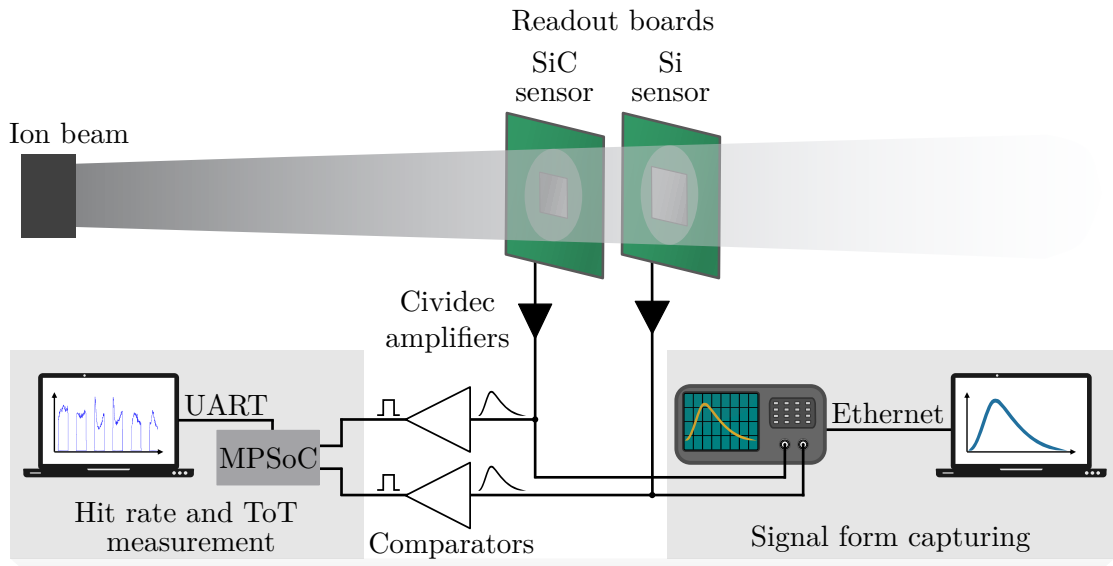


Figure 5.9: The measurement setup, which was used at MedAustron

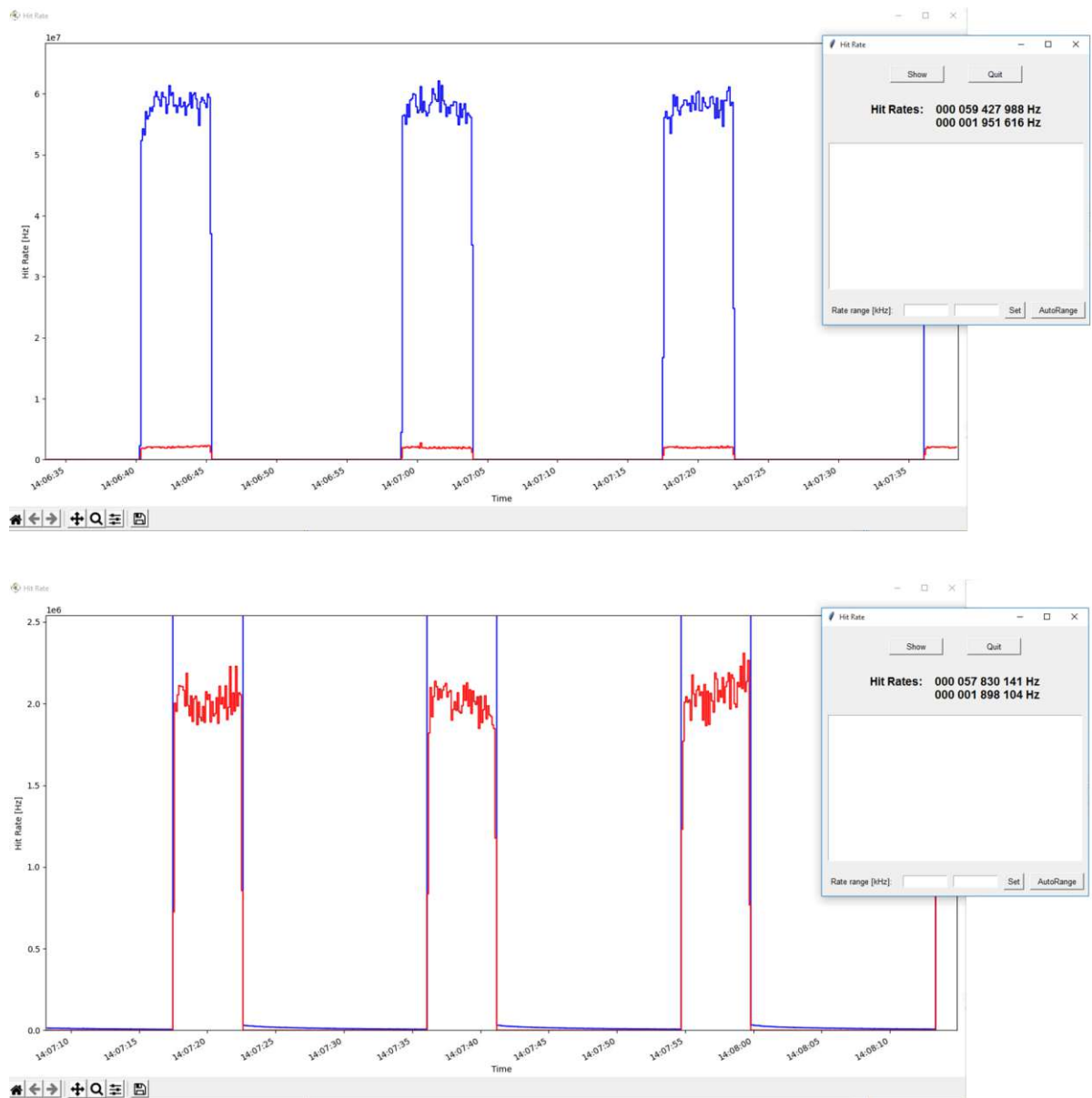


Figure 5.10: A screenshot of the program which receives and stores the FPGA data and calculates and displays the hit rates during data taking. Three Spills are shown. (blue: rate of silicon detector; red: rate of silicon carbide detector)

5.2.2 Results

The silicon amplitude histograms show for all beam energies a clear separation between a Landau and Gaussian distribution (Figure 5.11). As described in the Section 5.1.2, the entities belonging to the Gaussian are pure noise records, while the Landau elements are a superposition of signals produced by protons and noise. The gap between these two parts is shrinking for higher energies because of the decreasing energy deposition per path length at higher proton beam energies (as described in Section 2.1.3). For the 62.4 MeV beam energy, the Landau goes over into a nearly Gaussian function. This could result from the fact that the sensor thickness can no longer be seen as infinitely thin, which is required to produce a pure Landau distribution, or due to the fact that the amplification of the Cividec between input and output voltage is not linear above 1 V.

The silicon carbide sensor was used as the trigger to capture the silicon waveforms, but the SiC SNR is not sufficient to detect particles reliable in this setup (further discussed in the next paragraph). The result is that a considerable amount of records were just triggered by noise. By decreasing the beam energy, the SNR is increased, and as a consequence, the ratio of particle signal-to-noise triggers is growing. This can be seen in a rising ratio between entities belonging to the Landau and the Gaussian distribution.

The silicon carbide sensor amplitude histograms, triggered by the silicon sensor, almost show a Gaussian distribution (Figure 5.12). As shown in the results of the beta telescope setup (Figure 5.6), the distribution is a consequence of Gaussian noise, but in contrast to the MIP amplitude spectrum, a Landau tail is visible here. The tail is most pronounced for low beam energies, resulting from higher energy depositions at lower particle energies. The fusion of the Landau and the Gaussian distribution like seen here, makes it impossible to set a threshold with which all particle hits can be detected reliably. Therefore, in this setup with the silicon carbide sensor, the signal-to-noise ratio is not sufficient to detect particles unambiguously.

The average signal amplitude is proportional to the mean number of freed charge pairs produced by the penetrating particles. As described in Section 2.3.2 and Section 2.3.3, the proportionality factor depends on the charge carrier mobilities of the sensor material, the sensor capacitance and the readout system properties. Because of their proportionality, it is possible to perform a Bethe-Bloch curve fit with the amplitudes of the mean signals (Figure 5.13) for different beam energies (Figure 5.14). The results (Figure 5.13 and Figure 5.14) show that the mean amplitude values of silicon are around sixteen times higher than the ones measured with silicon carbide (14.3 for 100.4 MeV, 16.1 for 252.7 MeV and 17.1 for 800 MeV). This can partly be explained by the thickness difference ($189\ \mu\text{m}/45\ \mu\text{m} = 4.2$), the bandgap heights, and the resulting difference in pair production energies ($7.28\ \text{eV}/3.6\ \text{eV} \approx 2.02$) (material properties from Section 3.1 and Section 3.3). The rest is likely a result of the discrepancies in charge carrier mobilities and statistical deviations in the renormalization calculation of the SiC mean signals (see description of Figure 5.13). However, the comparison between the silicon and silicon carbide results should be made with caution. When used as a trigger, the low SNR of the SiC signals

could influence the Si waveform capturing in an unwanted way, distorting so the statistics.

The difference in the signal-to-noise ratio between silicon and silicon carbide detector can also be seen in the particle rate determination (Figure 5.15). While the rate measured by silicon is in good agreement with the known particle rates, the high setting rate at 62 MeV estimated by the SiC system is approximately four times lower. For higher energies equal to lower SNR, the difference between the Si and SiC rate grows. At the nominal setting, the silicon rate drifts with increasing degrader level away from the beam rates towards the silicon carbide rates. This could result from possible pile-ups (see Section 2.3.4), which omit a decrease of the signal between multiple particle hits below the lower threshold and thus prevent the recognition of every particle.

Silicon amplitudes in proton beam with different energies

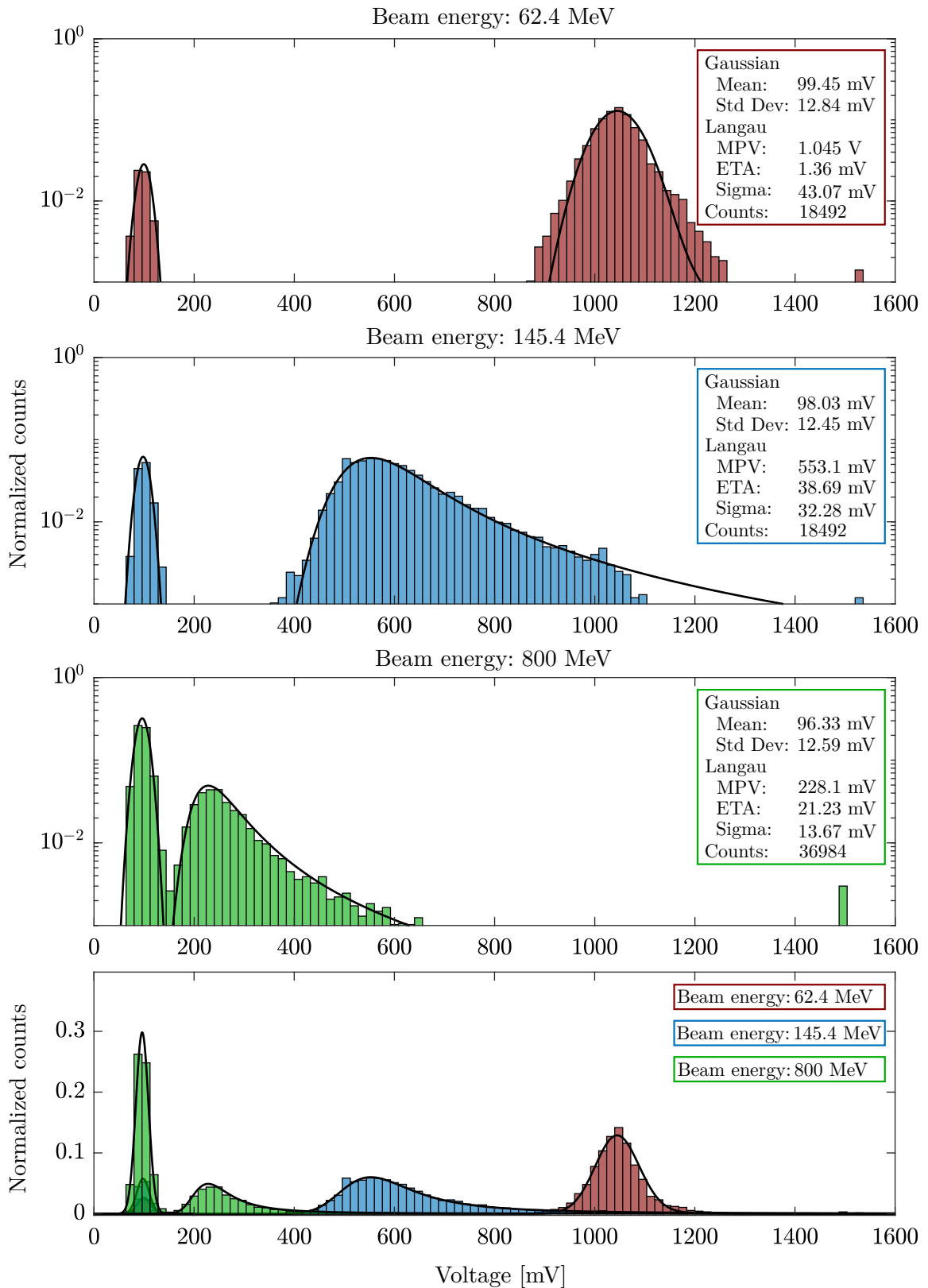


Figure 5.11: Shows the silicon sensor signal amplitude distributions for different beam energies. The waveform capturing was triggered by the silicon carbide sensor. Gaussians were fitted on the left and Langau functions on the right parts of the histograms. The corresponding fit parameters are shown in the graphs.

Silicon carbide amplitudes in proton beam with different energies

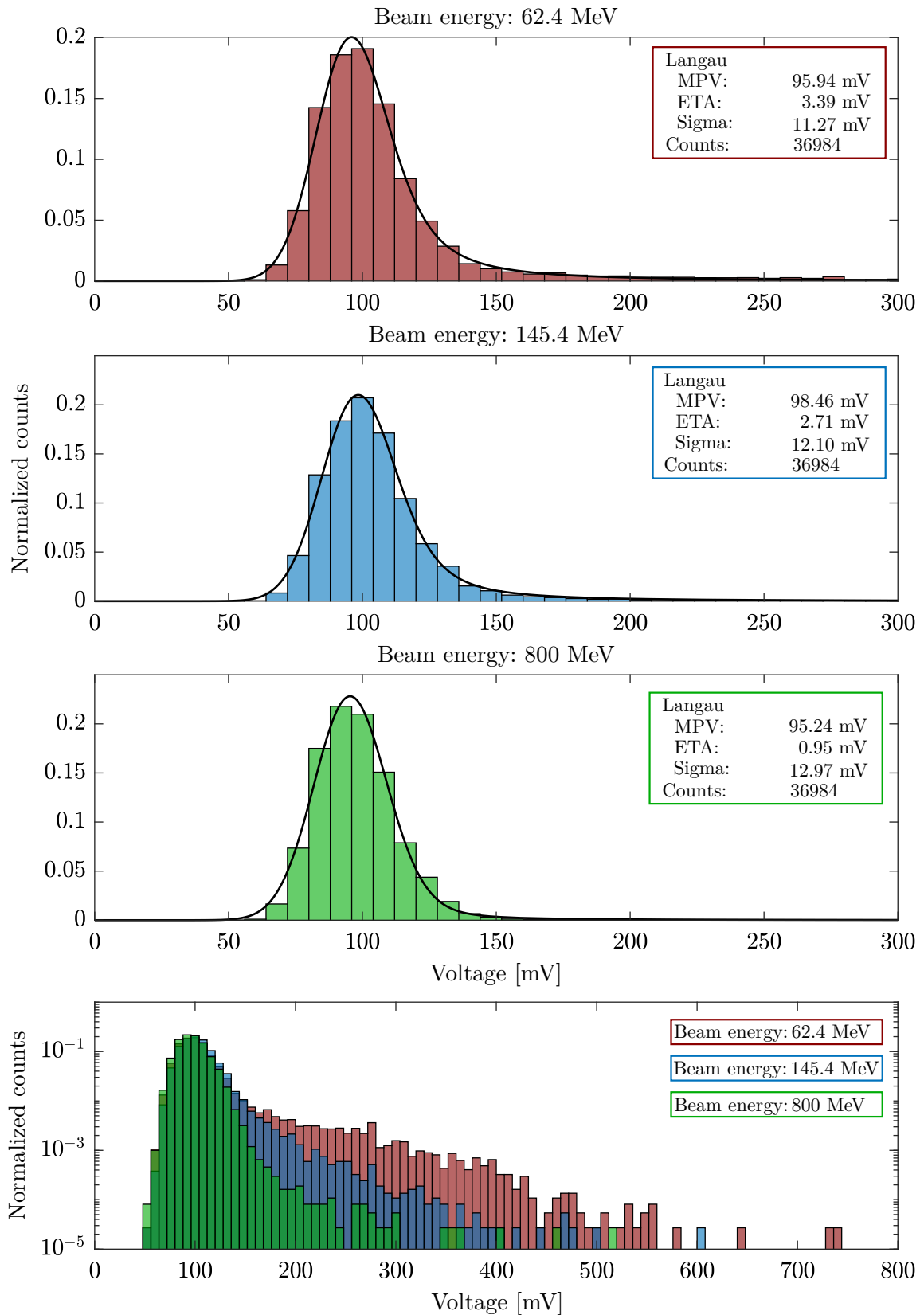


Figure 5.12: Shows the silicon carbide amplitude distributions measured in the beamline for different particle energies. The recording of the waveforms was triggered by the silicon sensor. A Langau was fitted upon the captured data.

Silicon and silicon carbide mean sensor signals for different beam energies

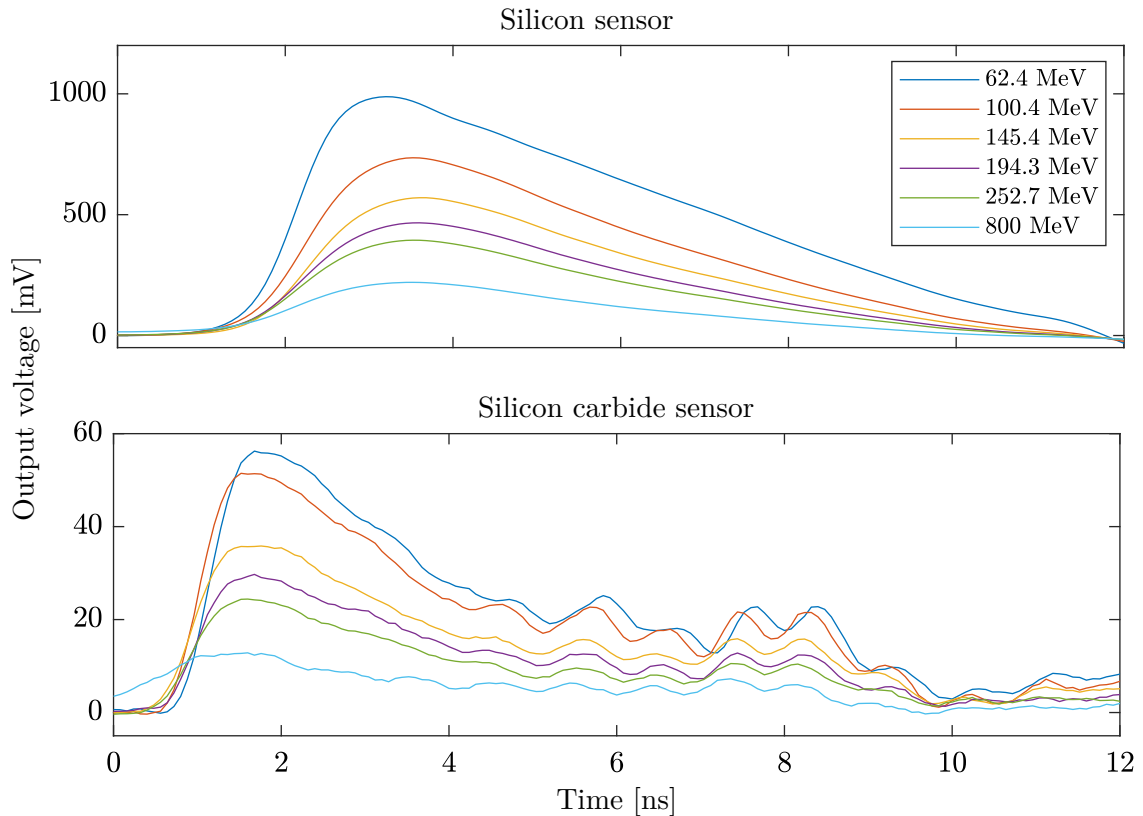


Figure 5.13: Shows the silicon and silicon carbide mean signals produced by different beam energies. In case of the silicon sensor, the signal form was determined by averaging over all waveforms entities belonging to the Langau distribution of Figure 5.11, excluding thereby pure noise signals. This separation cannot be done with the silicon carbide signals, so the averaging was done overall waveforms. Although the noise hits should cancel each other out, the resulting signal normalization is thereby altered. With a simulation of the setup in Gate (the same one as mentioned in Section 5.2.1), the probability was determined that if a particle hit the silicon sensor, it also hit the silicon carbide sensor. The silicon carbide signals were captured with the silicon sensor as trigger; therefore, this probability also defines the relative quantity of waveforms, including particle signals, statistically. By dividing the averaged waveform by the relative number of captured particle hits, the original mean signal was approximated. The results show that the noise is still visible.

Mean signal amplitudes of Si & SiC sensors with Bethe-Bloch fit

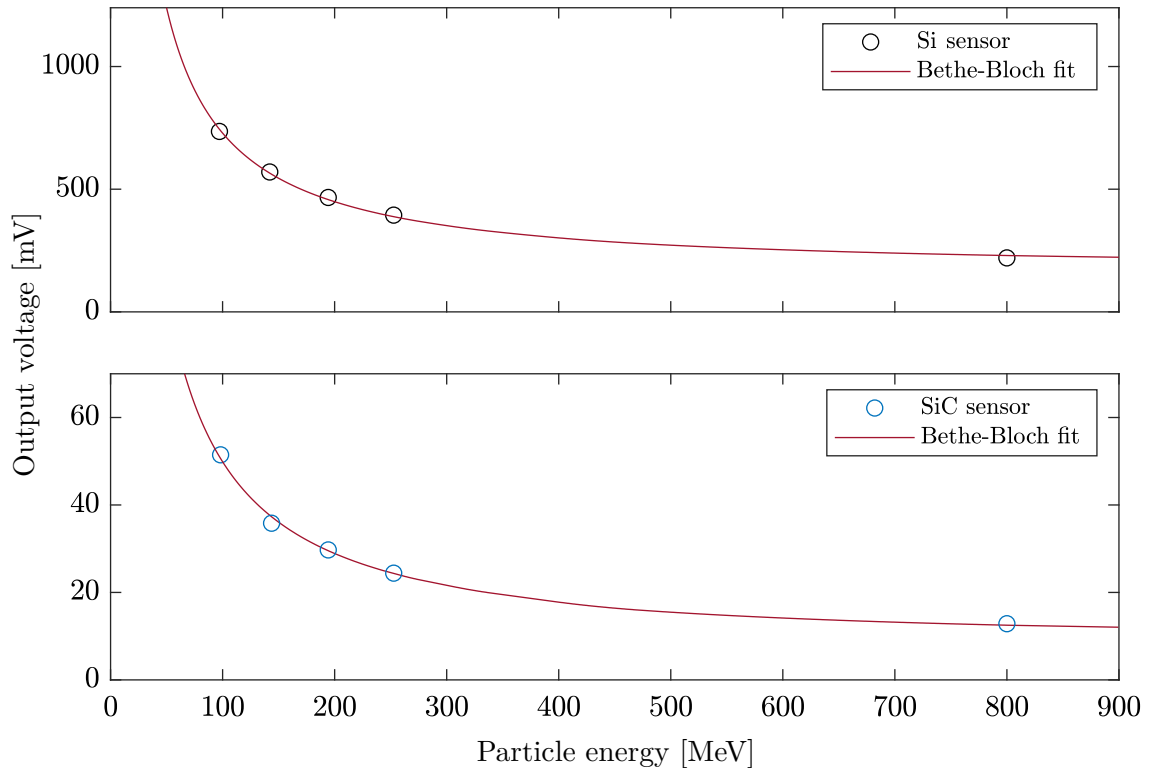


Figure 5.14: The points in the diagrams show the amplitudes of the waveform of Figure 5.13. The energy values on the x-axis mark the energies of the particles when they hit the corresponding sensor, not the beam energy setting. Those points were used to fit a Bethe-Bloch curve for silicon and silicon carbide.

Beam rates and extrapolated measured rates

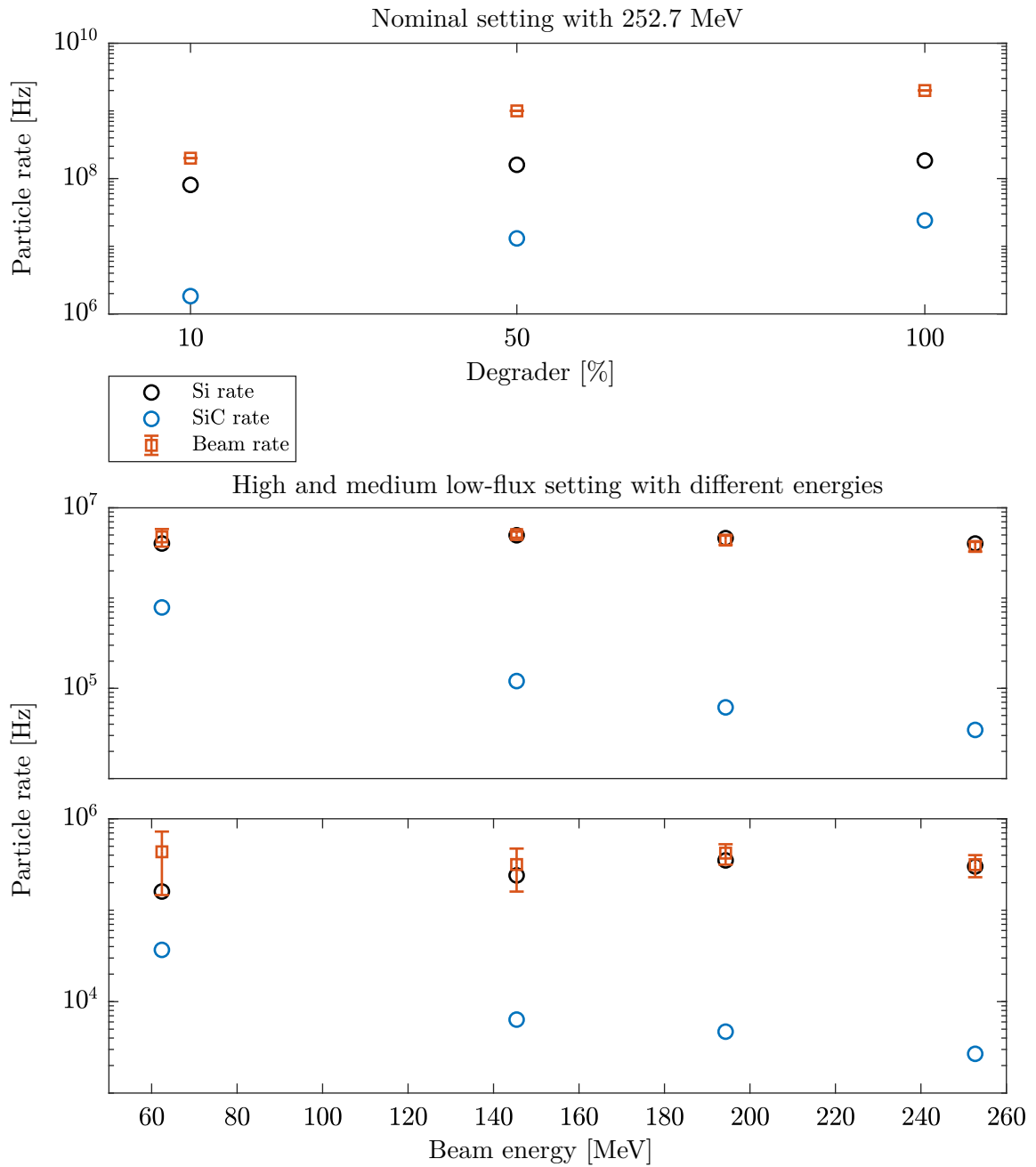


Figure 5.15: The Figure shows the extrapolated measured rates. To achieve better comparability, the measured rates were modified by a geometric factor. The results are the sensor rates, which would have been measured if the detector areas had encompassed the entire beam. The geometric factors were determined by the Gate simulation described in Section 5.2.1. (Beam rates kindly provided by [3])

6 Conclusion and outlook

In this project, three different detector materials, silicon, silicon carbide, and CVD diamond, were compared to study the possibility of using silicon carbide as a replacement for the currently used SFX scintillating at MedAustron and as a sensor material for the detection of high-intensity ion beams in general.

The simulations in Weightfield2 and the measurements at MedAustron show that the average silicon carbide signals are faster than the ones of silicon and diamond. This reduces the number of pile-up occurrences at high particle intensities and could explain, in addition to the smaller sensor area, why the silicon carbide rates for the nominal settings increase nearly proportional to the degrader configuration while the rates measured with the silicon sensor didn't.

The results also point out that the silicon carbide mean signal amplitudes are below the ones of silicon and diamond. But while the simulations of Weightfield2 suggest a silicon carbide amplitude half of the silicon amplitude size, the measurements in the proton beam indicate approx. sixteen times smaller amplitudes (see Figure 5.13). The results from the experiments with the alpha particle source suggest an even more notable difference, at least ten times smaller SiC signal, without even counting that the discrepancies in sensor thickness have here no effect. The differences between the various results could be explained as follow. A look into the source code of Weightfield uncovered that the program makes no distinction between Si and SiC when calculating the number of created charge pairs by a MIP particle. However, the deposited energy per path length insight the materials and the energies to make a charge pair are not the same. The consequence is a reduction of the amplitudes difference. Another explanation could be that the normalization of the SiC signals from the MedAustron measurements, used to determine the proportionality of sixteen, is also only an approximation. As described above, the low SNR of the silicon carbide signal could lead to the fact that only a specific type of silicon signals are being captured, altering so the signal statistics. A setup improvement would be to trigger the waveform capturing with a third sensor in the beamline, with a higher SNR like the LGAD of Section 3.4. Furthermore, the result of the Gate simulation was used to normalize the SiC signals, but it contains only an abstraction of the setup, and the resulting probability underlies statistical fluctuations.

Nevertheless, it can be concluded that the silicon carbide signal is, in any case, smaller than the silicon signal and even smaller than the diamond signal. At the highest beam energy, 800 MeV, the Gaussian noise distribution and the Langau particle signal distribution of the silicon sensor are just separable. This means that if the silicon carbide detector should detect all particles reliable at all beam energies, the signal amplitudes

must be increased and the noise decreased, to compensate in combination at least the proportionality factor between silicon and silicon carbide. Measurements in which the whole detector system was put into a metallic shielding box have shown that the noise is mainly produced by the electric circuit itself and not induced by external sources. Therefore, the next step is to examine the contribution to the noise of each component separately. With that, it is possible to look for alternatives for the most noise-producing elements. Also, an utterly new readout system based on the experience gained in this project is in planning. This system will be realized in an ASIC (application-specific integrated circuit). The integrated architecture could further decrease the noise introduced by the electronics. Other approaches, which could be applied in combination with the noise-reducing solutions, would be to increase the signal by expanding the 45 μm active zone, using the LGAD concept on a silicon carbide sensor, or raising the bias voltage.

To summarize, it can be stated that sensors made of silicon carbide could bring various advantages for applications with high-intensity beams, provided the signal-to-noise ratio is improved. However, this project's current silicon carbide detector setup doesn't produce the SNR to detect MIP particles reliably. So it can not be used at this point as a replacement for the SFX detectors at MedAustron.

7 Acknowledgement

I would like to thank Prof. Jochen Schieck, for giving me the opportunity to work on this interesting project.

I thank Thomas Bergauer for his supervision and support throughout the project, inspiring dedication to the subject, and patient guidance.

Moreover, I would like to thank all members of the HEPHY Detector Development group for assisting me wherever they could.

Here I especially thank Richard Thalmeier, Felix Ulrich-Pur, Verena Dangl, Patrick Sieberer and Max Tomaschek for their help during this study.

I also thank my parents and siblings for their encouraging words and support despite the distance lying between us.

And a special thanks go to my wife Marion for her continuous mental support, her valuable advice, honest criticism, and for being my source of tranquility during my thesis writing process.

Appendices

List of Figures

2.1	Particle scattering on atoms	4
2.2	Emission of bremsstrahlung in matter	4
2.3	Mean energy loss per path length for different materials and different particles	6
2.4	Bragg curve of silicon when interacting with α particles with initial energy of 5.486 MeV	7
2.5	Example of a Landau distribution	8
2.6	Bragg curve for different particles in water	9
2.7	Band structure of silicon	10
2.8	Different operation modes of a diode	11
2.9	Schematic illustration of a doped semiconductor strip sensor	12
2.10	Schematic illustration of the pile-up effect	15
2.11	The radioactive sources used in this project	16
2.12	Schematic illustration of the α decay	17
2.13	Radioactive decay scheme of Americium-241	17
2.14	Energy spectrum of Am-241 particles in 4 mm distance to the source . . .	18
2.15	Schematic illustration of the β^- decay	19
2.16	Strontium-90 energy spectrum	20
2.17	Energy spectrum of Strontium-90 particles after travelling through a PCB board with 1.60 mm thickness	20
2.18	Electron stopping power in silicon	21
3.1	A picture and a schematic illustration of the silicon diode used in this project	23
3.2	A picture and a schematic illustration of the CVD diamond used in this project	25
3.3	A picture and a schematic illustration of the silicon carbide diode used in this project	27
3.4	The structure of a planar LGAD sensor based on a silicon diode	28
3.5	The LGAD sensor, which is used in the beta telescope measurements . . .	28
3.6	The IV measurement setup	29
3.7	The CV measurement setup	30
3.8	The IV measurement results	30
3.9	The CV measurement results	31
3.10	The simulated electric potential and the simulated interaction with a MIP proton insight a silicon detector	33
3.11	The Weightfield2 simulation results	34
4.1	The UCSC board equipped with the silicon carbide sensor	35
4.2	The different layers of the UCSC PCB board	36

4.3	The schematic of the UCSC board transimpedance amplifier and the low supply voltage smoothing circuit	37
4.4	The Qucs UCSC board simulation circuit	40
4.5	The Qucs simulation results of the UCSC board	42
5.1	Measurement setup to capture signals produced by particles from the Am-241 source	45
5.2	The distributions of the α particle signal max. values for different bias voltages	46
5.3	An illustration of the used beta telescope setup	47
5.4	The beta telescope build up in the laboratory	48
5.5	The signal amplitude distribution of the silicon sensor for different bias voltages produced by MIP particles	49
5.6	The signal amplitude distribution of the silicon carbide sensor for different bias voltages produced by MIP particles	50
5.7	The signal amplitude distribution of the diamond sensor for different bias voltages produced by MIP particles	51
5.8	The available low flux settings at MedAustron	52
5.9	The measurement setup, which was used at MedAustron	54
5.10	A screenshot of the program which receives and stores the FPGA data and calculates and displays the hit rates during data taking	55
5.11	The silicon sensor signal amplitude distributions for different beam energies	58
5.12	The silicon carbide sensor signal amplitude distributions for different beam energies	59
5.13	The silicon and silicon carbide mean signals produced by different beam energies	60
5.14	Bethe-Bloch curve fit for the mean signal amplitudes of the silicon and silicon carbide sensor	61
5.15	The extrapolated rates measured with the silicon and silicon carbide sensor	62

List of Tables

3.1	The dark current and capacitance values of the silicon diode for different bias voltages	23
3.2	Different characteristics of the planar silicon diode	23
3.3	The dark current and capacitance values of the CVD diamond sensor for different bias voltages	25
3.4	The heights of the bandgap for different silicon carbide lattice structures .	26
3.5	Different characteristics of the silicon carbide diode	27
3.6	The dark current and capacitance values of the silicon carbide sensor for different bias voltages	27
4.1	The results of the readout board simulation done in Qucs	41
5.1	The oscilloscope trigger levels used in the Am-241 setup	44

Bibliography

- [1] R. R. WILSON, “Radiological use of fast protons.,” *Radiology*, vol. 47, no. 5, pp. 487–491, Nov. 1946, ISSN: 00338419. [Online]. Available: <https://pubs.rsna.org/doi/abs/10.1148/47.5.487>.
- [2] O. Jäkel, “Physical advantages of particles: protons and light ions,” *The British journal of radiology*, vol. 93, no. 1107, p. 20190428, Mar. 2020, ISSN: 1748880X. [Online]. Available: <https://www.birpublications.org/doi/10.1259/bjr.20190428>.
- [3] F. Ulrich-Pur *et al.*, “Commissioning of low particle flux for proton beams at MedAustron,” 2021. arXiv: 2102.06240v2.
- [4] F. H. Ruddy, A. R. Dulloo, J. G. Seidel, J. W. Palmour, and R. Singh, “The charged particle response of silicon carbide semiconductor radiation detectors,” in *Nuclear Instruments and Methods in Physics Research, Section A: Accelerators, Spectrometers, Detectors and Associated Equipment*, vol. 505, North-Holland, Jun. 2003, pp. 159–162.
- [5] —, “The charged particle response of silicon carbide semiconductor radiation detectors,” *Nuclear Instruments and Methods in Physics Research Section A: Accelerators, Spectrometers, Detectors and Associated Equipment*, vol. 505, no. 1-2, pp. 159–162, Jun. 2003, ISSN: 0168-9002.
- [6] M. Thomson, “1 Introduction,” eng, in *Modern particle physics*, 1. publ., Cambridge [u.a.]: Cambridge Univ. Press, 2013, pp. 1–29, ISBN: 1107034264.
- [7] H. Kolanoski and N. Wermes, “7 Gasgefüllte Detektoren,” in *Teilchendetektoren*, Springer Berlin Heidelberg, 2016, pp. 179–268.
- [8] —, “13 Szintillationsdetektoren,” in *Teilchendetektoren*, Springer Berlin Heidelberg, 2016, pp. 495–536.
- [9] —, “8 Halbleiterdetektoren,” in *Teilchendetektoren*, Springer Berlin Heidelberg, 2016, pp. 269–383.
- [10] —, “3 Wechselwirkungen von Teilchen mit Materie,” in *Teilchendetektoren*, Springer Berlin Heidelberg, 2016, pp. 27–90.
- [11] P. Sigmund, “Nuclear Stopping,” in *Stopping of Heavy Ions*, Jun. 2004, pp. 85–94.
- [12] P. A. Zyla *et al.*, “Review of Particle Physics,” *PTEP*, vol. 2020, no. 8, p. 083C01, 2020.
- [13] J. F. Ziegler, M. D. Ziegler, and J. P. Biersack, “SRIM - The stopping and range of ions in matter (2010),” *Nuclear Instruments and Methods in Physics Research, Section B: Beam Interactions with Materials and Atoms*, vol. 268, no. 11-12, pp. 1818–1823, Jun. 2010, ISSN: 0168583X.

- [14] R. Fosbinder and D. Orth, *Essentials of Radiologic Science*. Wolters Kluwer Health/Lippincott Williams & Wilkins, 2011, ISBN: 9780781775540. [Online]. Available: <https://books.google.at/books?id=jRVg5i1M1UEC>.
- [15] U. Schneider, E. Pedroni, and A. Lomax, “The calibration of CT Hounsfield units for radiotherapy treatment planning,” *Physics in Medicine and Biology*, vol. 41, no. 1, pp. 111–124, Jan. 1996, ISSN: 00319155. [Online]. Available: <https://iopscience.iop.org/article/10.1088/0031-9155/41/1/009%20https://iopscience.iop.org/article/10.1088/0031-9155/41/1/009/meta>.
- [16] M. Yang *et al.*, “Comprehensive analysis of proton range uncertainties related to patient stopping-power-ratio estimation using the stoichiometric calibration,” *Physics in Medicine and Biology*, vol. 57, no. 13, pp. 4095–4115, Jul. 2012, ISSN: 00319155. [Online]. Available: <https://pubmed.ncbi.nlm.nih.gov/22678123/>.
- [17] F. Ulrich-Pur *et al.*, “Imaging with protons at MedAustron,” *Nuclear Instruments and Methods in Physics Research, Section A: Accelerators, Spectrometers, Detectors and Associated Equipment*, vol. 978, p. 164 407, Oct. 2020, ISSN: 01689002. arXiv: 2003.00115.
- [18] L. I. Berger, *Semiconductor Materials*. Taylor & Francis, 1996, ISBN: 9780849389122. [Online]. Available: https://books.google.de/books?id=Ty5Ymlg%5C_Mh0C.
- [19] J. Chelikowsky, “Silicon in all its forms,” *MRS Bulletin*, vol. 27, no. 12, pp. 951–960, Jan. 2002, ISSN: 08837694. [Online]. Available: www.mrs.org/publications/bulletin.
- [20] Cepheiden; Wikimedia Commons. “Band structure Si schematic.” (2015), [Online]. Available: https://commons.wikimedia.org/wiki/File:Band_structure_Si_schematic.svg?uselang=de.
- [21] H. Kolanoski and N. Wermes, “4 Bewegung von Ladungsträgern in elektrischen und magnetischen Feldern,” in *Teilchendetektoren*, Springer Berlin Heidelberg, 2016, pp. 91–129.
- [22] —, “5 Signalentstehung durch bewegte Ladungen,” in *Teilchendetektoren*, Springer Berlin Heidelberg, 2016, pp. 131–162. [Online]. Available: https://link.springer.com/chapter/10.1007/978-3-662-45350-6_5.
- [23] M. Kafaee, A. Moussavi Zarandi, and A. Taheri, “Neural-based pile-up correction and ballistic deficit correction of X-ray semiconductor detectors using the Monte Carlo simulation and the Ramo theorem,” *Radiation Effects and Defects in Solids*, vol. 171, no. 3-4, pp. 271–278, Mar. 2016, ISSN: 10294953.
- [24] M. F. L’Annunziata, “Alpha Radiation,” in *Radioactivity : introduction and history*, Elsevier, Jan. 2007, pp. 71–84.
- [25] G. Audi, F. G. Kondev, M. Wang, W. J. Huang (’@w, and S. Naimi, “The NUBASE2016 evaluation of nuclear properties *,” *Chinese Physics C*, vol. 41, no. 3, p. 30 001, 2017. [Online]. Available: <http://amdc.impcas.ac.cn/>.

- [26] M. Berger, J. Coursey, M. Zucker, and J. Chang, *ESTAR, PSTAR, and ASTAR: Stopping-Power and Range Tables for Electrons, Protons, and Helium Ions*. [Online]. Available: <https://www.nist.gov/pml/stopping-power-range-tables-electrons-protons-and-helium-ions> (visited on 05/01/2021).
- [27] I. Henins, "Precision density measurement of silicon," *Journal of Research of the National Bureau of Standards Section A: Physics and Chemistry*, vol. 68A, no. 5, p. 529, Sep. 1964, ISSN: 0022-4332. [Online]. Available: [/pmc/articles/PMC6628575/](https://pmc/articles/PMC6628575/) <https://www.ncbi.nlm.nih.gov/pmc/articles/PMC6628575/?report=abstract> <https://www.ncbi.nlm.nih.gov/pmc/articles/PMC6628575/>.
- [28] M. Michalek, "GATE simulations on silicon-sensor testing using radioactive sources," no. June, 2021.
- [29] M. F. L'Annunziata, "Beta Radiation," in *Radioactivity : introduction and history*, Elsevier, Jan. 2007, pp. 119–140.
- [30] J. Dixon *et al.*, "Evaluation of a Silicon ⁹⁰Sr Betavoltaic Power Source," *Scientific Reports*, vol. 6, no. 1, pp. 1–6, Dec. 2016, ISSN: 20452322. [Online]. Available: www.nature.com/scientificreports.
- [31] R. D. Ryan, "Precision measurements of the ionization energy and its temperature variation in high purity silicon radiation detectors," *IEEE Transactions on Nuclear Science*, vol. 20, no. 1, pp. 473–480, 1973.
- [32] N. D. Arora, J. R. Hauser, and D. J. Roulston, "Electron and Hole Mobilities in Silicon as a Function of Concentration and Temperature," *IEEE Transactions on Electron Devices*, vol. 29, no. 2, pp. 292–295, 1982.
- [33] C. J. Wort and R. S. Balmer, "Diamond as an electronic material," *Materials Today*, vol. 11, no. 1-2, pp. 22–28, Jan. 2008, ISSN: 1369-7021.
- [34] M. Pomorski *et al.*, "Characterisation of single crystal CVD diamond particle detectors for hadron physics experiments," *physica status solidi (a)*, vol. 202, no. 11, pp. 2199–2205, Sep. 2005, ISSN: 1862-6319. [Online]. Available: <https://onlinelibrary.wiley.com/doi/full/10.1002/pssa.200561929> <https://onlinelibrary.wiley.com/doi/abs/10.1002/pssa.200561929> <https://onlinelibrary.wiley.com/doi/10.1002/pssa.200561929>.
- [35] W. de Boer *et al.*, "Radiation hardness of diamond and silicon sensors compared," *Physica Status Solidi (A) Applications and Materials Science*, vol. 204, no. 9, pp. 3004–3010, May 2007. arXiv: 0705.0171. [Online]. Available: <https://arxiv.org/abs/0705.0171v1>.
- [36] H. Pernegger *et al.*, "Charge-carrier properties in synthetic single-crystal diamond measured with the transient-current technique," *J. Appl. Phys.*, vol. 97, no. 7, pp. 73704–1–9, Apr. 2005. [Online]. Available: <https://cds.cern.ch/record/909063>.

- [37] S. M. Hearne, E. Trajkov, D. N. Jamieson, J. E. Butler, and S. Prawer, "The role of charge trapping at grain boundaries on charge transport in polycrystalline chemical vapor deposited diamond based detectors," *Journal of Applied Physics*, vol. 99, no. 11, p. 113 703, Jun. 2006, ISSN: 0021-8979. [Online]. Available: <https://aip.scitation.org/doi/abs/10.1063/1.2194116>.
- [38] S. Mersi, E. Borch, M. Bruzzi, R. D'Alessandro, S. Lagomarsino, and S. Sciortino, "A study of charge collection processes on polycrystalline diamond detectors," *Nuclear Instruments and Methods in Physics Research Section A: Accelerators, Spectrometers, Detectors and Associated Equipment*, vol. 530, no. 1-2, pp. 146–151, Sep. 2004, ISSN: 0168-9002.
- [39] H. Yoneda, K. Tokuyama, R. Yamazaki, K.-i. Ueda, H. Yamamoto, and K. Baba, "Effect of grain boundaries on carrier lifetime in chemical-vapor-deposited diamond film," *Applied Physics Letters*, vol. 77, no. 10, p. 1425, Aug. 2000, ISSN: 0003-6951. [Online]. Available: <https://aip.scitation.org/doi/abs/10.1063/1.1308054>.
- [40] H. Matsunami, "Technological Breakthroughs in Growth Control of Silicon Carbide for High Power Electronic Devices," *Japanese Journal of Applied Physics*, vol. 43, no. 10R, p. 6835, Oct. 2004, ISSN: 1347-4065. [Online]. Available: <https://iopscience.iop.org/article/10.1143/JJAP.43.6835><https://iopscience.iop.org/article/10.1143/JJAP.43.6835/meta>.
- [41] S. Metzger, H. Henschel, O. Köhn, and W. Lennartz, "Silicon carbide radiation detector for harsh environments," *IEEE Transactions on Nuclear Science*, vol. 49 III, no. 3, pp. 1351–1355, Jun. 2002.
- [42] J. B. Casady and R. W. Johnson, "Status of silicon carbide (SiC) as a wide-bandgap semiconductor for high-temperature applications: A review," *Solid-State Electronics*, vol. 39, no. 10, pp. 1409–1422, Oct. 1996, ISSN: 0038-1101.
- [43] M. V. S. Chandrashekar, C. I. Thomas, and M. G. Spencer, "Measurement of the mean electron-hole pair ionization energy in 4H SiC," *Applied Physics Letters*, vol. 89, no. 4, p. 042 113, Jul. 2006, ISSN: 0003-6951. [Online]. Available: <https://aip.scitation.org/doi/abs/10.1063/1.2243799>.
- [44] A. A. Lebedev, A. M. Ivanov, and N. B. Strokan, "Radiation Resistance of SiC and Nuclear-Radiation Detectors Based on SiC Films," *Semiconductors*, vol. 38, no. 2, pp. 125–147, Feb. 2004.
- [45] S. K. Chaudhuri, K. J. Zavalla, and K. C. Mandal, "Experimental determination of electron-hole pair creation energy in 4H-SiC epitaxial layer: An absolute calibration approach," *Applied Physics Letters*, vol. 102, no. 3, p. 031 109, Jan. 2013, ISSN: 0003-6951. [Online]. Available: <https://aip.scitation.org/doi/abs/10.1063/1.4776703>.
- [46] C. Poole and I. Darwazeh, "11 Microwave semiconductor materials and diodes," in *Microwave Active Circuit Analysis and Design*, Academic Press, Jan. 2015, pp. 355–393, ISBN: 978-0-12-407823-9.

- [47] N. Moffat *et al.*, “Low Gain Avalanche Detectors (LGAD) for particle physics and synchrotron applications,” in *Journal of Instrumentation*, vol. 13, Institute of Physics Publishing, Mar. 2018, p. C03014. [Online]. Available: <https://doi.org/10.1088/1748-0221/13/03/C03014>.
- [48] N. Cartiglia, *Weightfield2*. [Online]. Available: [http://personalpages.to.infn.it/~%5Csim\\$cartigli/Weightfield2/](http://personalpages.to.infn.it/~%5Csim$cartigli/Weightfield2/) (visited on 07/20/2021).
- [49] *UcscSingleChannel < Main < TWiki*. [Online]. Available: <https://twiki.cern.ch/twiki/bin/view/Main/UcscSingleChannel> (visited on 07/15/2021).
- [50] *Qucs project: Quite Universal Circuit Simulator*. [Online]. Available: <http://qucs.sourceforge.net/index.html> (visited on 09/12/2021).
- [51] V. Dangl, “Evaluation of an FPGA-Module for the application in a particle detector readout system,” 2021.
- [52] J. S *et al.*, “GATE V6: a major enhancement of the GATE simulation platform enabling modelling of CT and radiotherapy,” *Physics in medicine and biology*, vol. 56, no. 4, pp. 881–901, Feb. 2011, ISSN: 1361-6560. [Online]. Available: <https://pubmed.ncbi.nlm.nih.gov/21248393/>.
- [53] *Geant4*. [Online]. Available: <https://geant4.web.cern.ch/> (visited on 08/17/2021).

Eidesstattliche Erklärung

Hiermit erkläre ich, dass ich die vorliegende Arbeit gemäß dem Code of Conduct - Regeln zur Sicherung guter wissenschaftlicher Praxis, insbesondere ohne unzulässige Hilfe Dritter und ohne Benutzung anderer als der angegebenen Hilfsmittel, angefertigt wurde. Die aus anderen Quellen direkt oder indirekt übernommenen Daten und Konzepte sind unter Angabe der Quelle gekennzeichnet. Die Arbeit wurde bisher weder im In- noch im Ausland in gleicher oder in ähnlicher Form in anderen Prüfungsverfahren vorgelegt.

Wien, 12.09.2021


.....
Manuel Christanell